Firing-rate resonance in a generalized integrate-and-fire neuron with subthreshold resonance

Nicolas Brunel,[1] Vincent Hakim,[2] and Magnus J. E. Richardson[2,3]

[1]*Neurophysique et Physiologie du Système Moteur (CNRS UMR 8119), Université Paris René Descartes, 45 rue des Saints Pères, 75270 Paris Cedex 06, France*

[2]*Laboratoire de Physique Statistique,* Ecole Normale Supérieure, 24 rue Lhomond, 75231 Paris Cedex 05, France*

[3]*Laboratory of Computational Neuroscience, Brain and Mind Institute, Ecole Polytechnique Fédérale de Lausanne, CH-1015, Lausanne, Switzerland*

(Received 20 December 2002; published 19 May 2003)

Neurons that exhibit a peak at finite frequency in their membrane potential response to oscillatory inputs are widespread in the nervous system. However, the influence of this subthreshold resonance on spiking properties has not yet been thoroughly analyzed. To this end, generalized integrate-and-fire models are introduced that reproduce at the linear level the subthreshold behavior of any given conductance-based model. A detailed analysis is presented of the simplest resonant model of this kind that has two variables: the membrane potential and a supplementary voltage-gated resonant variable. The firing-rate modulation created by a noisy weak oscillatory drive, mimicking an *in vivo* environment, is computed numerically and analytically when the dynamics of the resonant variable is slow compared to that of the membrane potential. The results show that the firing-rate modulation is shaped by the subthreshold resonance. For weak noise, the firing-rate modulation has a *minimum* near the preferred subthreshold frequency. For higher noise, such as that prevailing *in vivo*, the firing-rate modulation *peaks* near the preferred subthreshold frequency.

DOI: 10.1103/PhysRevE.67.051916 PACS number(s): 87.19.La, 05.40.−a, 87.19.Nn

I. INTRODUCTION

Advances in recordings, in visualization techniques, and in computational modeling capabilities [1,2] have made notable progress possible towards the understanding of the dynamics of neural assemblies. Neuronal synchronization and oscillations have been studied *in vivo* and *in vitro* in slices of neural tissues and analyzed theoretically with the help of computer simulations [3]. The properties of the single cell and of the synaptic couplings between different cells are both thought to play a role in the observed dynamics. In particular, it has been found that the subthreshold membrane potential response of neurons subjected to a small oscillatory drive depends on the drive frequency and can be peaked at particular frequencies. Examples include trigeminal root ganglion neurons [4], neocortical neurons [5,6], hippocampal pyramidal cells [7,8] and interneurons [8], and others [9]. It has long been known that this resonance phenomenon can be related to the neuronal ionic channel characteristics and can be accurately modeled using the classic Hodgkin-Huxley conductance-based description [10,11]. In order to assess the functional significance of this subthreshold resonance, it is important to determine its relation to spike emission, and particularly to examine the case of a neuron embedded in a neural structure under heavy synaptic bombardment, as is the case *in vivo*. In a previous paper [12], numerical simulations of conductance-based models under noisy oscillatory drive were performed to address this question. It was found that, for a sufficient level of noise, the modulation of the spike rate at the driving frequency was related to the subthreshold resonance curve. The classic Lapicque or leaky integrate-and-fire (IF) model [13,14] has been useful for understanding in simple terms the properties of more detailed spiking neuron models and of real neurons and neuronal networks [15–17]. However, the leaky integrate-and-fire model cannot describe subthreshold resonance. This motivated the introduction [12,18] of a generalized integrate-and-fire (GIF) model to describe more accurately these types of subthreshold properties. As for conductance-based models, the spike rate resonance curve of the GIF model was found to be peaked at the firing-rate frequency for low noise and around the subthreshold resonance for stronger noise regimes.

The aim of the present work is to present an analytic computation of the spike rate modulation and phase for the GIF model and a detailed analysis of the findings of Ref. [12]. The GIF model and its relation to linearized conductance-based models are first recalled in Sec. II. The main characteristics of the model for constant input or weak oscillatory drive without noise are given in Sec. III. The general perturbative framework of the computation for noisy inputs and the main results are then described in Sec. IV. They are first explained using a simple but representative case in Sec. IV A. The general lowest-order computation is then dealt with in Sec. IV B. It is found here that a sufficient level of noise is necessary for the subthreshold resonance to be seen in the firing-rate modulation. This interplay of noise and oscillations is reminiscent of stochastic resonance [19]. However, as discussed in Sec. IV C, the two phenomena are quite different since, for instance, the usual leaky IF model displays stochastic resonance [20] but not the subthreshold and firing-rate resonance studied here. A discussion of the results and some perspectives of the present work are provided in the concluding section. The results of some higher-order computations are described in the Appendix.

*Associé au CNRS et aux Universités Paris VI et VII.

II. SUBTHRESHOLD DYNAMICS AND THE GIF MODEL

A. Subthreshold response of conductance-based models

The response of neurons to a small oscillatory current has been tested in a number of experiments. In several cases, a peak response has been observed at a frequency that depends on the particular neuron type under examination. This resonance phenomenon is well accounted for by the conductance-based description of a single compartment neuron. In this classic Hodgkin-Huxley description [10,11], with an injected current $I_{app}(t)$, the potential difference across the cell membrane $V=V_{in}-V_{out}$ is given by

$$C\frac{dV}{dt}=g_L(E_L-V)-\sum_j I_j(V,\{x_k\})+I_{app}(t), \qquad (1)$$

where C denotes the membrane capacity, g_L and E_L are the conductance and reversal potential of a passive leak current, the I_j's are a set of ionic currents associated with active conductances (by convention, positive values are associated with outward currents), and I_{app} is the externally applied current. The I_j's are generally taken to be functions of the potential and of N additional activation and inactivation variables $\{x_k, k=1,\cdots,N\}$, with time course

$$\frac{dx_k}{dt}=\frac{x_k^\infty(V)-x_k}{\tau_k(V)}, \qquad (2)$$

where both the relaxation times $\tau_k(V)$ and the steady-state values x_k^∞ depend on V. For a small injected current $I_{app}(t)$, the departure $v(t)$ of the membrane potential from its resting value V_0 is described by the linearized version of Eqs. (1) and (2)

$$C\frac{dv}{dt}=-gv-\sum_k g_k w_k+I_{app}(t),$$

$$\tau_k\frac{dw_k}{dt}=v-w_k, \quad k=1,\ldots,N, \qquad (3)$$

where g is the sum of all the steady-state conductances, τ_k is the relaxation time of x_k at the resting potential, $\tau_k=\tau_k(V_0)$, and g_k measures the strength of the steady-state current flow change due to the x_k variation following a small modification of the steady-state potential value,

$$g=g_L+\sum_j \partial I_j/\partial V|_{V_0},$$

$$g_k=\sum_j \left.\frac{\partial I_j}{\partial x_k^\infty}\right|_{V_0}\left.\frac{dx_k^\infty}{dV}\right|_{V_0}. \qquad (4)$$

Variable w_k measures the departure of the activation or inactivation variable x_k from its value at the steady-state potential,

$$w_k=\frac{x_k-x_k^\infty(V_0)}{\left.\frac{dx_k^\infty}{dV}\right|_{V_0}}. \qquad (5)$$

Without variables w_k, Eq. (3) is equivalent to a simple electric RC circuit. In this case, the amplitude of the potential oscillation induced by an injected alternating current decreases monotonically with the frequency of the current. Variables w_k add effective inductances into this electric circuit analogy and can give rise to a nonmonotonic frequency response curve. Adding a single w_k is already sufficient to produce a peak response [9], a resonance, at a particular frequency and more complex responses can be obtained with several variables [12].

B. The GIF model

The effect of a subthreshold resonance on the spike rate can be directly examined by supplementing the subthreshold dynamics (3) with a threshold for spike emission in the spirit of the usual leaky integrate-and-fire neuron description [14,2]. That is, a GIF model is defined by using Eq. (3) as long as the potential v is below a threshold θ. When v reaches θ, a spike emission is registered, v is reset to a lower value V_r and the linear evolution (3) resumes [18]. In principle, the supplementary variables w_k could also be reset at the spike emission time when $v=\theta$. For simplicity, it is chosen here to leave them unaffected. This is appropriate for variables that have slow dynamics relative to the spike duration and it has also the advantage of keeping to a minimum the number of parameters in the model. In neural structures, a neuron receives a continuous barrage of inputs arriving at a large number of synapses. This is modeled here as a constant mean injected current I_0 plus a fluctuating Gaussian part $\eta(t)$ of amplitude Δ, $\langle\eta(t)\eta(t')\rangle=\Delta\delta(t-t')$. We thus consider the following two-variable GIF model:

$$C\frac{dv}{dt}=-gv-g_1w+I_0+\eta(t)+I_{osc}(t), \quad v<\theta \qquad (6)$$

$$\tau_1\frac{dw}{dt}=v-w, \qquad (7)$$

where $I_{osc}(t)$ is a small oscillating test current. When v reaches θ, it is instantaneously reset to $V_r<\theta$. The noise strength is more intuitively measured by the amplitude σ_V of membrane potential fluctuations than by Δ. Without the threshold condition, the two are easily related

$$\sigma_V^2=\langle(v-\langle v\rangle)^2\rangle=\frac{\Delta}{2C}\frac{C+g\tau_1+g_1\tau_1}{(g+g_1)(C+g\tau_1)}. \qquad (8)$$

An example of the dynamics is shown in Fig. 1.

The present study focuses on computing the spike rate in this model with the particular aim of analyzing the influence of the subthreshold resonance on the input-output transfer function for this neuron. In the presence of a small oscillating input current $I_{osc}(t)=\hat{I}/2\exp(i\omega t)+$c.c., the instanta-

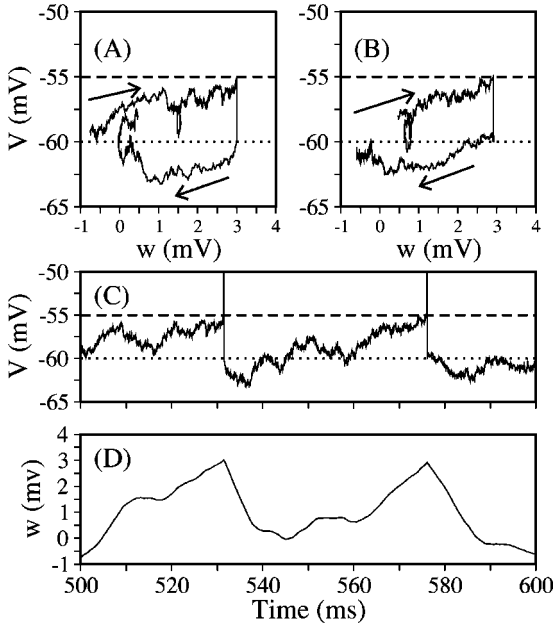

FIG. 1. An example of the variation of voltage v and auxiliary variable w as a function of time for a GIF neuron [$C/g_1=10$ ms, $g_1/g=10$, $\tau_1=10$ ms, $I_0/g_1=1$ mV, and $\Delta/Cg_1=5(\mathrm{mV})^2$]. (a) Evolution in the v versus w plane for time 500 to 550 ms. (b) Evolution in the v versus w plane for time 550–600 ms. (c) Voltage v as a function of time. Spikes are indicated by vertical lines for clarity. (d) Auxiliary variable w as a function of time. For illustrative purposes, all voltages have been shifted by -60 mV, such that for this case the rest and reset (dotted line) are at -60 mV ($V_r=0$ mV) and the threshold for spike emission is at -55 mV ($\theta=5$ mV).

neous firing-rate $r(t)$, averaged over a population of independent neurons or over many trials for a single neuron, shows a weak modulation

$$r(t)=r_s+\frac{1}{2}[\hat{r}(\omega)\hat{I}\exp(i\omega t)+\text{c.c.}], \tag{9}$$

where r_s is the time-independent spike rate in the absence of the weak drive (c.c. stands for the complex conjugate terms). Modulation $\hat{r}(\omega)$, or signal gain (e.g., Ref. [21]), measures the amplification of the frequency ω in the output signal and its phase. It is one of the main factors determining synchronization at the network level [17]. It will be computed in the following sections under various conditions, in order to determine when and how it is modified by subthreshold resonance.

Before considering the effect of noise, the main characteristics of the deterministic two-variable GIF model are described.

III. THE DETERMINISTIC GIF MODEL

A. Subthreshold dynamics of the two-variable model

The subthreshold dynamics of the two-variable model is identical to the dynamics of a general two-variable conductance-based model for small excursions around some holding voltage.

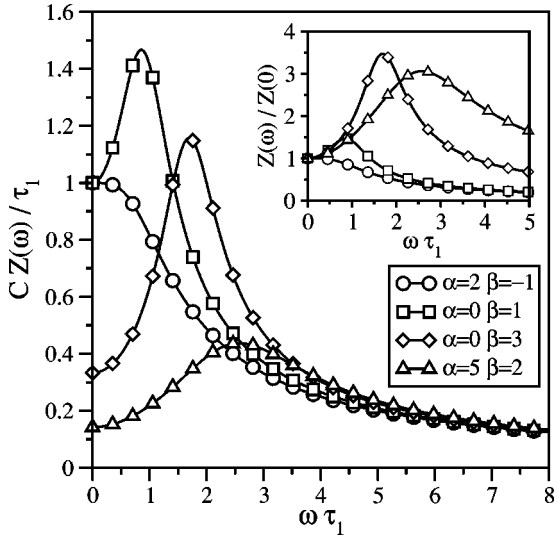

FIG. 2. Several subthreshold resonance curves. The magnitude of the impedance $|Z|$ is displayed as a function of frequency. The four different curves correspond to the four parameter points marked with the corresponding symbols in Fig. 3. The inset shows the impedance magnitude after normalization by its value at zero frequency. For $\alpha=0$, the relative strength of the resonance peak increases with β, as seen by comparing the curves marked by squares and diamonds.

1. Steady-state stability

In the two-variable case, the dynamics depends on the dimensionless ratios $\alpha=\tau_1 g/C$ and $\beta=\tau_1 g_1/C$. For a constant injected current $I_{app}=I_0$, one can rewrite Eq. (3) by using τ_1 as the time unit as

$$\frac{dv}{dt}=-\alpha v-\beta w+I_0\tau_1/C, \tag{10}$$

$$\frac{dw}{dt}=v-w. \tag{11}$$

The steady-state $v=w=I_0/(g+g_1)$ exists for $I_0<(g+g_1)\theta$. The exponential relaxation (or growth) of perturbations is controlled by the two eigenvalues $\xi_\pm$, which obey

$$\xi^2+(\alpha+1)\xi+\alpha+\beta=0. \tag{12}$$

The steady state is therefore stable when both eigenvalues have a real negative part, i.e., when $\alpha+1>0$ and $\alpha+\beta>0$.

2. Subthreshold resonance

In this parameter domain where the resting state is stable, the injection of a small alternating current $I_{osc}(t)=\hat{I}/2\exp(i\omega t)+\text{c.c.}$ induces oscillations around the resting membrane potential, $v(t)=I_0/(g+g_1)+1/2[\hat{V}\exp(i\omega t)+\text{c.c.}]$. An elementary computation gives $\hat{V}=Z(\omega)\hat{I}$ with

$$Z(\omega)=\frac{\tau_1}{C}\frac{1+i\omega}{\beta+(1+i\omega)(\alpha+i\omega)}. \tag{13}$$

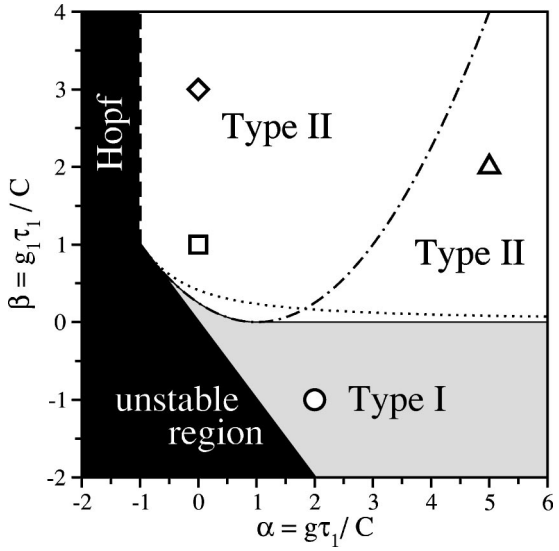

FIG. 3. The phase diagram of the GIF model in the $\alpha = g\tau_1/C, \beta = g_1\tau_1/C$ parameter plane. Models in the black region have no stable rest state. Models represented by parameters above the dotted line have a subthreshold resonance. Those above the dashed-dotted line have complex eigenvalues $\xi_\pm$. As explained in the text, models in the gray region are of type I, whereas those in the white region are of type II. The subthreshold resonance curves of the models corresponding to the points marked by the different symbols (circle, triangle, square, diamond) are drawn in Fig. 2.

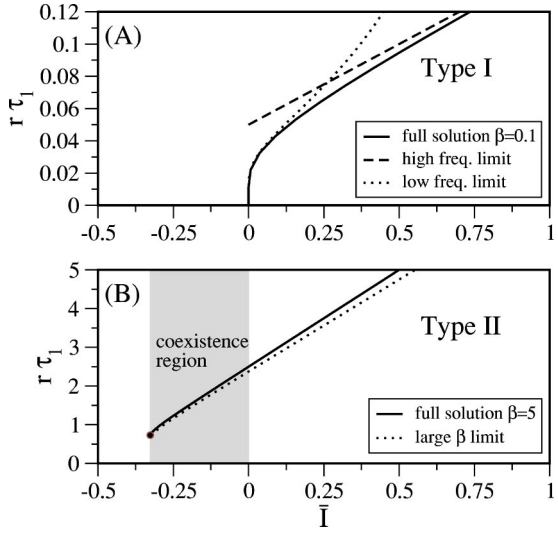

FIG. 4. Firing rates $r_s(I)$ as a function of the normalized injected current $\bar{I} = (I_0/g_1 - \theta)/(\theta - V_r)$ for two zero-leak GIF models ($g=0$) with different β parameters. The full lines correspond to the exact firing rates as given by Eq. (17). Top panel: type-I model with $\beta = 0.1$. The low frequency approximation of Eq. (18) (dotted line) is shown as well as the high frequency approximation $r_s\tau_1 = \beta(\bar{I} + 1/2)$ (dashed line). Bottom panel: type-II model with $\beta = 5$. The dotted line corresponds to the large β approximation Eq. (20) and the shaded area is the region in which a quiescent and a firing state coexist.

The response amplitude $|Z(\omega)|$ displays a peak at a finite nonzero frequency ω_p (Fig. 2) when $\beta^2 + 2\beta + 2\alpha\beta > 1$ with

$$\omega_p = \sqrt{(\beta^2 + 2\beta + 2\alpha\beta)^{1/2} - 1}. \tag{14}$$

The parameter domain where $|Z(\omega)|$ displays a peak at finite frequency overlaps with domain $\beta > (\alpha - 1)^2/4$, where Eq. (12) has complex roots but the two are different (see Fig. 3), as noted previously [12].

An especially simple case is obtained for zero leak ($g = 0$ or $\alpha = 0$). The model then only depends on the dimensionless ratio $\beta = \tau_1 g_1 / C$. The steady state is stable for $\beta > 0$ and Eq. (12) has complex eigenvalues for $\beta > 1/4$. A resonant response occurs in the more restricted case, when the time scale of the supplementary variable w is sufficiently slow, for $\beta > \sqrt{2} - 1$. The resonant peak grows with β. In particular, for $\beta \gg 1$, the maximal response amplification, $Q = |Z(\omega_p)/Z(0)|$, is equal to β at the peak frequency $\omega_p \sim \sqrt{\beta}$ and the peak width is of order $1 \ll \omega_p$.

3. Periodic firing regimes

In order to analyze the GIF-neuron firing rate and its dependence on current I_0, periodic firing regimes (i.e., limit cycles) are now considered. Between a reset of the potential at $v = V_r$ and the next spike emission when v reaches θ a period T later, the dynamics is a simple superposition of exponentials controlled by the two eigenvalues $\xi_\pm$,

$$v = \frac{I_0}{g + g_1} + a\exp(\xi_+ t) + b\exp(\xi_- t),$$

$$w = \frac{I_0}{g + g_1} + \frac{a}{1 + \xi_+}\exp(\xi_+ t) + \frac{b}{1 + \xi_-}\exp(\xi_- t). \tag{15}$$

The constants a, b are determined by requiring that v starts from V_r at $t = 0$ and ends at θ at $t = T$. They are given in term of period T as

$$a = \frac{1}{\exp(\xi_+ T) - \exp(\xi_- T)}\left[\left(\theta - \frac{I_0}{g + g_1}\right) - e^{\xi_- T}\left(V_r - \frac{I_0}{g + g_1}\right)\right],$$

$$b = \frac{-1}{\exp(\xi_+ T) - \exp(\xi_- T)}\left[\left(\theta - \frac{I_0}{g + g_1}\right) - e^{\xi_+ T}\left(V_r - \frac{I_0}{g + g_1}\right)\right]. \tag{16}$$

Since w is not modified when a spike is emitted, the period T is obtained by the periodicity condition $w(0) = w(T)$, which gives

$$\frac{I_0}{g + g_1} = V_r + \frac{\theta - V_r}{\xi_+ - \xi_-}\left\{\frac{1 + \xi_+}{1 - \exp(\xi_+ T)} - \frac{1 + \xi_-}{1 - \exp(\xi_- T)}\right\}. \tag{17}$$

The solutions of Eq. (17) correspond to periodic solutions where v goes from V_r to θ during period T, that is to neurons periodically emitting spikes at a rate $r_s(I_0) = 1/(\tau_1 T)$ in di-

mensional units. However, the condition that $v(t)$ should remain below θ during its motion has not been taken into account in Eq. (17). Among the solutions of Eq. (17), only those which satisfy this condition correspond to real solutions. The simpler zero-leak case is analyzed first.

(*a*) *The zero-leak case* ($\alpha=0$). In the parameter range $0<\beta<1/4$, the two eigenvalues $\xi_\pm$ are real and negative, $\xi_-<-1/2<\xi_+<0$. For $T\to+\infty$, the slower relaxation dominates and Eq. (17) can be approximately written as

$$\frac{I_0}{g_1}-\theta\simeq\frac{\theta-V_r}{\xi_+-\xi_-}(1+\xi_+)\exp(\xi_+T). \tag{18}$$

The right-hand-side (rhs) of Eq. (18) is positive, so a periodic state appears above the threshold $I_0/g_1=\theta$ with a logarithmically long period $T\sim|\ln(I_0/g_1-\theta)|$. This is a kind of type-I behavior, analogous to that of the usual IF neuron.

The situation is different for $\beta>1/4$ when the two eigenvalues are complex $\xi_\pm=-1/2\pm i\xi_2$. Then, Eq. (17) reads, for $T\to+\infty$,

$$\frac{I_0}{g_1}-\theta\simeq(\theta-V_r)\exp(-T/2)\left[\cos(\xi_2T)+\frac{\sin(\xi_2T)}{2\xi_2}\right]. \tag{19}$$

The rhs in Eq. (19) oscillates and takes both positive and negative signs for T large while decaying to zero. Thus, solutions to Eq. (17) exist below $I_0/g_1=\theta$. The smallest solution T of Eq. (17) gives a potential $v(t)$ that remains below θ and corresponds to a real periodic regime. So, for $\beta>1/4$, a steady and a periodically firing state coexist in a range of applied currents: a type-II behavior. The firing rate as a function of applied current is displayed in Fig. 4, for several values of β. The domain of coexistence and the firing-rate are easily estimated for $\beta\gg1$. Then $\xi_2\sim\sqrt{\beta}, T\sim1/\sqrt{\beta}$, and expansion of Eq. (17) in inverse powers of β gives

$$\frac{I_0}{g_1}=\frac{\theta+V_r}{2}+\frac{\theta-V_r}{4\xi_2}\left[\cot(\xi_2T/2)+\frac{\xi_2T/2}{\sin^2(\xi_2T/2)}\right]. \tag{20}$$

The expression within square brackets on the rhs of Eq. (20) attains its minimum for $\xi_2T=\pi$. So, for large β, the steady periodically firing state coexists with the steady-state in the interval

$$\frac{V_r+\theta}{2}+\frac{(\theta-V_r)\pi}{8\sqrt{\beta}}+\cdots\leqslant\frac{I_0}{g_1}\leqslant\theta. \tag{21}$$

It appears at the lower end of the interval with the finite period $T\simeq\pi/\sqrt{\beta}$. The lower bound $(V_r+\theta)/2$ in Eq. (21) can easily be understood. When $\beta\to+\infty$, the dynamics of the w variable is much slower than the dynamics of the potential and w simply relaxes to the average of v. For a constant w, the dynamics of v is linear in time and the mean of v in a periodically firing state is simply the average between the reset and threshold potentials. Putting $w=(\theta+V_r)/2$ in Eq. (10) immediately gives that a periodically firing state exists only if I_0/g_1 is larger than $(\theta+V_r)/2$. The period (with τ_1 as the time unit) in the same limit is simply obtained as

$$T\simeq\frac{C(\theta-V_r)}{\tau_1[I_0-g_1(\theta+V_r)/2]}\quad\text{for}\quad\beta\gg1, \tag{22}$$

which corresponds to Eq. (20) for $T\xi_2\ll1$.

(*b*) *The general non-zero-leak case* ($\alpha\neq0$). When $\alpha\neq0$, a similar analysis can be performed and is briefly summarized here. When $T\to+\infty$, Eq. (17) gives back the threshold $I_0=(g+g_1)\theta$. Two types of behavior can be distinguished by considering how I_0 departs from $(g+g_1)\theta$ for $T\gg1$: (1) the periodic state exists only for $I_0>(g+g_1)\theta$ and starts with infinite period at the threshold $I_0=(g+g_1)\theta$, i.e., a type-I behavior, or (2) a periodic state coexists with the steady state for some range of current below the threshold $I_0=(g+g_1)\theta$, i.e., a type-II behavior. In the parameter range $(\alpha-1)^2>4\beta$, $\xi_{+,-}$ are real and negative (with $\xi_-<\xi_+$). For large T, the slower relaxation ξ_+ dominates and Eq. (17) gives

$$\frac{I_0}{g+g_1}-\theta\simeq\frac{\theta-V_r}{\xi_+-\xi_-}(1+\xi_+)\exp(\xi_+T). \tag{23}$$

The neuron is of type I when the prefactor of the exponential in Eq. (23) is positive whereas it is of type II when the prefactor is negative.

The prefactor has the same sign as $1+\xi_+$. It is positive for $\beta<0$ as well as for $\beta>0$ and $\alpha<1$ and negative for $\beta>0$, $\alpha>1$.

In the parameter range $(\alpha-1)^2<4\beta$, ξ_+ and ξ_- are complex conjugates and the obtained correction in the analog of Eq. (17) is oscillatory. This indicates the existence of periodic firing regimes below $I_0/(g+g_1)$ and correspond to type-II behavior.

The region of type-II behavior exactly corresponds to the parameter region delimited in Ref. [12], where after a current step, the membrane potential overshoots before relaxing to the new holding potential. The different regions are displayed in Fig. 3. It should be noted that in general the type-II behavior does not necessarily correspond to the existence of complex roots: a difference of exponentials can provide the overshoot leading to type-II behavior.

4. Firing-rate resonance

In this section, the firing-rate modulation by a small time-varying current is considered. The analysis is limited to the computation of the linear response. It amounts to generalizing the well-known analysis for the IF neuron [22] to the slightly more complicated two-variable GIF model. The aim is to investigate how the subthreshold resonance modifies the rate response function.

The neuron is submitted to the injected current $I_0+I_{osc}(t)$. The constant current I_0 is sufficiently large, so that in the absence of $I_{osc}(t)$ the neuron emits spikes periodically at times $t=nT+t_0, n=\ldots,-1,0,1,\ldots$. For a collection of

neurons, t_0 varies independently from neuron to neuron and the spike emission probability per unit time, r_s, is time independent. The effect of the small time-varying component is to slightly displace the spike times from t to $t+d(t)$.[1] This produces a modulation in time of the spike rate,

$$r(t)=r_s[1-d'(t)]. \tag{24}$$

In order to obtain the rate modulation, it remains to determine $d(t)$ for the two-variable GIF model. With an injected current with a small time-varying component, Eq. (10) becomes

$$\frac{dv}{dt}=-\alpha v-\beta w+[I_0+I_{osc}(t)]\tau_1/C. \tag{25}$$

At the linear level, the time-varying current can be decomposed in Fourier components and it is sufficient to consider $[I_{osc}(t)=\hat{I}/2\ \exp(i\omega t)+\text{c.c}]$. A particular solution to Eqs. (25) and (11) is given by

$$(v=1/2\ [(\hat{I}\tau_1/C)v_p\exp(i\omega_t)+\text{c.c}],$$
$$w=1/2[(\hat{I}\tau_1/C)w_p\exp(i\omega_t)+\text{c.c.}]),$$

with

$$v_p(\omega)=\frac{1+i\omega}{(1+i\omega)(\alpha+i\omega)+\beta},$$

$$w_p(\omega)=\frac{1}{(1+i\omega)(\alpha+i\omega)+\beta}. \tag{26}$$

Function $v_p=Z(\omega)C/\tau_1$ is a dimensionless form of the impedance $Z(\omega)$. Between the nth spike at time t_n and the $(n+1)$th spike at time t_{n+1}, the complete solution can be written as

$$v=\frac{I_0}{g+g_1}+a_n\exp[\xi_+(t-t_n)]+b_n\exp[\xi_-(t-t_n)]$$
$$+\frac{1}{2}[(\hat{I}\tau_1/C)v_p\exp(i\omega t)+\text{c.c.}], \tag{27}$$

$$w=\frac{I_0}{g+g_1}+\frac{a_n}{1+\xi_+}\exp[\xi_+(t-t_n)]$$
$$+\frac{b_n}{1+\xi_-}\exp[\xi_-(t-t_n)]$$
$$+\frac{1}{2}[(\hat{I}\tau_1/C)w_p\exp(i\omega t)+\text{c.c.}]. \tag{28}$$

The forcing perturbs $a_n, b_n, t_{n+1}-t_n$ and $w(t_n)$, the value of $w(t)$ at the spike time, away from their steady limit cycle values. At linear order, one can write

$$a_n=a+1/2\ [(\hat{I}\tau_1/C)\hat{a}\exp(i\omega t_n)+\text{c.c.}],$$

$$b_n=b+1/2[(\hat{I}\tau_1/C)\hat{b}\exp(i\omega t_n)+\text{c.c.}],$$

$$w(t_n)=w_0+1/2[(\hat{I}\tau_1/C)\hat{w}\exp(i\omega t_n)+\text{c.c.}],$$

and

$$t_{n+1}-t_n=T+1/2[(\hat{I}\tau_1/C)\hat{T}\exp(i\omega t_n)+\text{c.c.}].$$

The nth spike time t_n and the value of w at t_n determine the constants a_n and b_n in the time interval $[t_n, t_{n+1}]$, i.e., they give $\hat{a}$ and $\hat{b}$ as linear functions of $\hat{w}$ and $\hat{T}$. The knowledge of a_n and b_n in turn determines the $(n+1)$th spike time and the value $w(t_{n+1})$. This provides two supplementary equations that determine $\hat{w}$ and $\hat{T}$.

Explicitly, one obtains

$$\hat{a}=\frac{1}{\xi_--\xi_+}[(1+\xi_+)v_p+(1+\xi_+)(1+\xi_-)(\hat{w}-w_p)], \tag{29}$$

$$\hat{b}=\frac{1}{\xi_+-\xi_-}[(1+\xi_-)v_p+(1+\xi_+)(1+\xi_-)(\hat{w}-w_p)]. \tag{30}$$

Then $\hat{T}$ is determined by the condition that the $(n+1)$th spike occurs when v reaches θ,

$$\hat{T}=-\frac{\hat{a}\exp(\xi_+T)+\hat{b}\exp(\xi_-T)+v_p\exp(i\omega T)}{a\xi_+\exp(\xi_+T)+b\xi_-\exp(\xi_-T)}$$
$$=\kappa_1(\hat{w}-w_p)+\kappa_2 v_p, \tag{31}$$

where the two constants κ_1 and κ_2 are given by

[1] At this linear level, locking phenomena, which exist for any finite amplitude around resonances, are neglected. This limits the applicability of the linear response in this purely deterministic setting. The obtained response curve is nevertheless useful to describe the spike rate modulation as shown by Fig. 5 and to understand the small noise limit of Eq. (6).

$$\kappa_1=\frac{(1+\xi_+)(1+\xi_-)[\exp(\xi_-T)-\exp(\xi_+T)]}{[a\xi_+\exp(\xi_+T)+b\xi_-\exp(\xi_-T)][\xi_--\xi_+]}, \tag{32}$$

$$\kappa_2=\frac{(1+\xi_-)\exp(\xi_-T)-(1+\xi_+)\exp(\xi_+T)+(\xi_+-\xi_-)\exp(i\omega T)}{[a\xi_+\exp(\xi_+T)+b\xi_-\exp(\xi_-T)][\xi_--\xi_+]}. \tag{33}$$

This gives the evolution of w from one spike to the next,

$$\hat{w}\exp(i\omega T)=\lambda_L\hat{w}+\mu v_p+[\exp(i\omega T)-\lambda_L]w_p, \tag{34}$$

with

$$\lambda_L=\frac{(a\xi_++b\xi_-)\exp[(\xi_++\xi_-)T]}{a\xi_+\exp(\xi_+T)+b\xi_-\exp(\xi_-T)}, \tag{35}$$

$$\mu=\frac{\dfrac{a\xi_+}{1+\xi_+}\exp(\xi_+T)[\exp(\xi_-T)-\exp(i\omega T)]+\dfrac{b\xi_-}{1+\xi_-}\exp(\xi_-T)[\exp(\xi_+T)-\exp(i\omega T)]}{a\xi_+\exp(\xi_+T)+b\xi_-\exp(\xi_-T)}. \tag{36}$$

Equation (34) expresses $w(t_{n+1})$ (its lhs) as a function of $w(t_n)$ and the effective forcing on w, $[\mu v_p+(1-\lambda_L)w_p]$, coming from the imposed oscillating current (its rhs). In the absence of forcing, constant λ_L controls the free evolution of small perturbations around the limit cycle: it is the discrete Lyapunov exponent giving the (unforced) limit cycle stability. Equation (34) determines $\hat{w}$ as

$$\hat{w}=\frac{\mu v_p+[\exp(i\omega T)-\lambda_L]w_p}{\exp(i\omega T)-\lambda_L}. \tag{37}$$

Substituting this expression back in Eq. (31) with formulas (32)–(36) for the constants, gives the simple expression of $\hat{T}$,

$$\hat{T}=v_p(\omega)\left[\frac{a\xi_+\exp(\xi_+T)}{\exp(\xi_+T)-\exp(i\omega T)}+\frac{b\xi_-\exp(\xi_-T)}{\exp(\xi_-T)-\exp(i\omega T)}\right]^{-1}, \tag{38}$$

where T is given by Eq. (17) and a and b are given by Eq. (16) or by the equivalent formulas

$$a=-\frac{(\theta-V_r)(1+\xi_+)}{[\xi_+-\xi_-][1-\exp(\xi_+T)]},$$

$$b=-\frac{(\theta-V_r)(1+\xi_-)}{[\xi_--\xi_+][1-\exp(\xi_-T)]}. \tag{39}$$

These expressions permit a comparison of the zero frequency limit of Eq. (38) with a direct differentiation of Eq. (17) and a check that

$$\hat{T}(\omega=0)=\frac{C}{\tau_1}\frac{dT}{dI_0}. \tag{40}$$

After determining the variation $\hat{T}$ of the interspike interval, the time displacement of the nth spike at linear order follows by summation,

$$d(t_n)=\frac{\hat{I}\tau_1}{2C}\sum_{m=-\infty}^{n-1}\{\hat{T}\exp[i\omega(mT+t_0)]+\text{c.c.}\}$$

$$=\frac{\hat{I}\tau_1}{2C}\left[\frac{\hat{T}}{\exp(i\omega T)-1}\exp(i\omega t_n)+\text{c.c.}\right]. \tag{41}$$

As usual, the summation is performed by supposing that the perturbation is created slowly, that is, by adding a small negative imaginary part to the forcing frequency ω.

Finally, when the spike rate is written as $r_s+1/2[\hat{I}\hat{r}\exp(i\omega t)+\text{c.c.}]$ [Eq. (9)], the modulation amplitude $\hat{r}$ is obtained as

$$\frac{\hat{r}}{r_s}=-\frac{\tau_1}{C}\left(\frac{i\omega}{\exp(i\omega T)-1}\right)\hat{T}, \tag{42}$$

where $\hat{T}$ is explicitly given by Eq. (38). Expressions (38) and (42) generalize to the two-variable GIF model, the well-known formula [22] for the usual IF model. It is recovered for $\beta=0$ when the additional variable has no influence on the membrane potential dynamics. In this case, one has $\xi_+=-\alpha$ and $\xi_-=-1$ so that $b=0$ [Eq. (39)]. Equation (38) with $v_p=1/(\alpha+i\omega)$, then reads $\hat{T}\propto(1-\exp[(\alpha+i\omega)T])/(\alpha+i\omega)$, which gives back Knight's formula [22].

Equation (42) is plotted in Fig. 5 together with the results of direct numerical simulations for two cases where the GIF model displays subthreshold resonance. As for the usual leaky IF model, sharp resonance peaks are seen for frequencies that are multiples of the firing-rate. They arise from the vanishing of the denominator in formula (42). However, in this deterministic case, the GIF firing-rate resonance curve

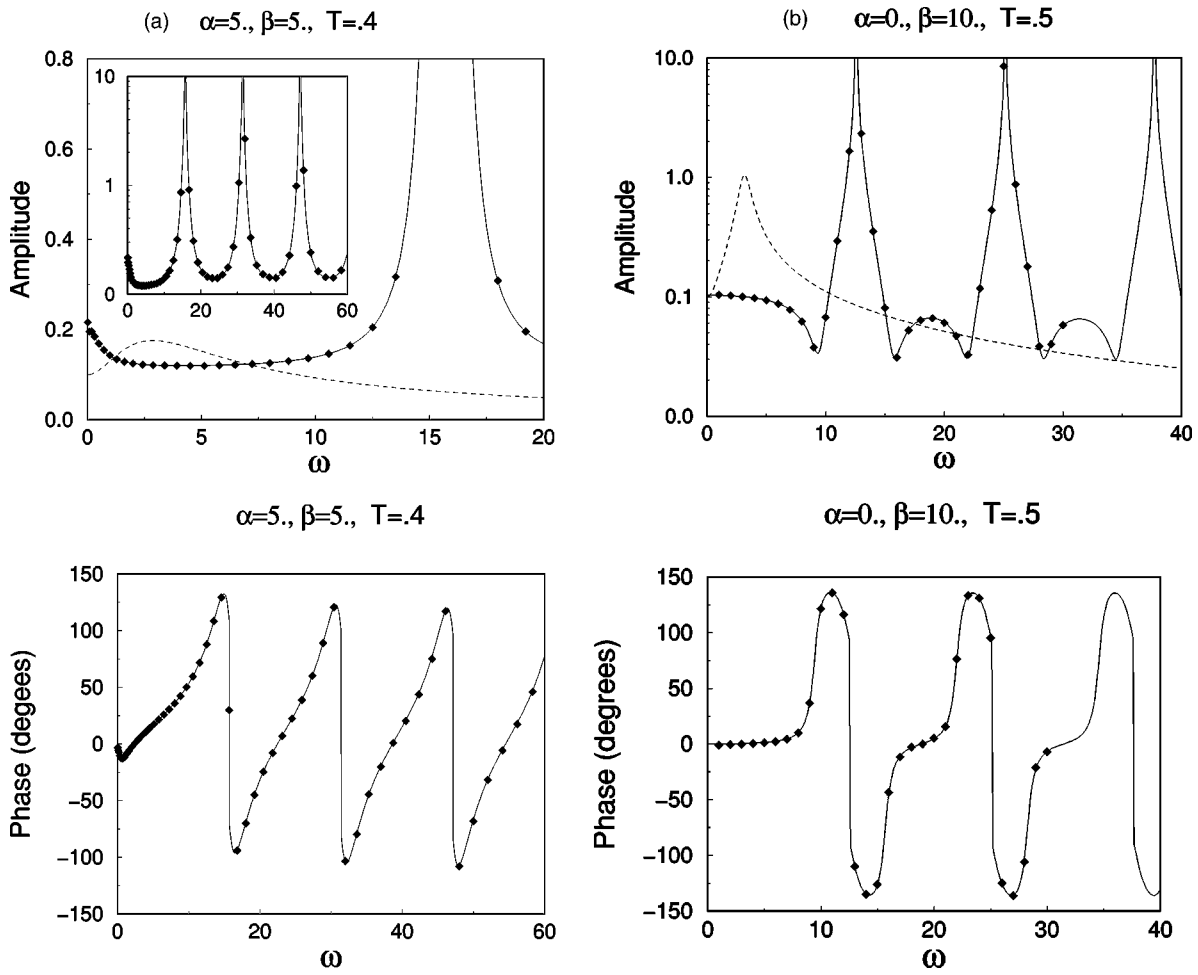

FIG. 5. Firing-rate resonance curves for the deterministic two-variable GIF model with $\theta=10$ mV, $V_r=5$ mV. The amplitude $|C\hat{r}/\tau_1 r_s|$ and phase of $\hat{r}$ are plotted for (a) $\alpha=5$, $\beta=5$, $T=0.4$ and (b) $\alpha=0$, $\beta=10$, $T=0.5$ (which, respectively, correspond to firing rates of 25 Hz and 20 Hz for $\tau_1=100$ ms). The solid lines represent the analytic result of Eq. (42). The diamonds show the results of numerical simulations of Eqs. (25) and (11) with a simple Euler code ($dt=1.0\times10^{-4}\tau_1$) and different forcing frequencies ω [(a) $I_0\tau_1/C=95.5325$ mV, $I_1\tau_1/C=0.2$ mV and (b) $I_0\tau_1/C=85.0975$ mV, $I_1\tau_1/C=0.2$ mV]. For each frequency, the dynamics was simulated for a total time of $t=5\times10^4\tau_1$. The modulation $\hat{r}/r_s$ was obtained as the average $\hat{r}/r_s=2C/(I_1\tau_1)\langle\exp(-i\omega t_n)\rangle$ computed over all occurring spike times t_n. The plotted amplitude and phase correspond to those of $\hat{r}/r_s$. The modulus of the subthreshold resonance curve $C|Z(\omega)/\tau_1|=|v_p|$ is also shown for comparison (dashed lines).

has no peak at the subthreshold resonance frequency. For $g\neq0$, it exhibits instead a suppression around the subthreshold resonance frequency.

For comparison with the following sections, the limiting form of $\hat{r}$ when τ_1 is long in comparison with other time scales is worth noting. Then, the dynamics of w does not play a significant role in most of the driving frequency range. Explicit expressions can be obtained by taking the limits of the above expressions when $\alpha,\beta\to+\infty, T\to0$ with α/β and βT fixed. For $g\neq0$, one obtains the expression for a usual IF neuron with leak conductance g and a resonance peak of well-defined limiting form around the firing-rate frequency. The limit is not uniform in a low frequency range that tends to zero with τ_1 (where the slow dynamics of w does play a role). The zero-leak case is special in that the firing-rate resonance curve of the allied zero-leak IF model has no peak at the firing-rate frequency [22]. For $g=0$, one obtains, in the limit $\tau_1\to+\infty$ with ωT fixed,

$$\frac{\hat{r}}{r_s}=\frac{T\tau_1}{C(\theta-V_r)}\left\{1+\frac{\beta T^2}{[1-\exp(i\omega T)]^2}\right\}. \tag{43}$$

For any finite $1/\tau_1$, the firing-rate response exhibits resonance peaks centered on the firing-rate frequency and its harmonics. However, the firing-rate response is modified by these resonances only in frequency intervals of width tending to zero such as $\sqrt{g_1/\tau_1 C}$ (in dimensional units) as $\tau_1\to+\infty$ (i.e., for $|\omega T-2\pi n|\sim\sqrt{\beta}T$).

IV. STEADY AND MODULATED SPIKE RATES WITH NOISY INPUTS

In a number of previous studies [14,16,17,23–25] on neuron firing-rates and modulation using the IF model with

noise, it has been found convenient to transform the stochastic description of neuron dynamics into a Fokker-Planck equation for the distribution of its membrane potential. In the present case, Eqs. (6) and (7) give a Fokker-Planck equation for the distribution $P(v,w,t)$ of the membrane potential and the supplementary variable w,

$$\partial_t P = \frac{1}{C}\partial_v[(gv + g_1 w - I_0 - I_{osc}(t))P] + \frac{1}{\tau_1}\partial_w[(w-v)P] + \frac{\Delta}{2C^2}\partial_v^2 P, \tag{44}$$

with an absorbing boundary condition at threshold $P(\theta,w,t)=0$. At the reset potential $v=V_r$ the distribution is continuous, but it has a discontinuous first derivative arising from the reinjected probability current

$$\partial_v P(v,w,t)|_{v=V_r^+} - \partial_v P(v,w,t)|_{v=V_r^-} = \partial_v P(v,w,t)|_{v=\theta}. \tag{45}$$

The instantaneous firing-rate $r(t)$ is simply related to the total probability current through the threshold,

$$r(t) = -\frac{\Delta}{2C^2}\int_{-\infty}^{+\infty} dw\, \partial_v P(\theta,w,t). \tag{46}$$

Without the threshold condition, the stationary solution $[I_{osc}(t)=0]$ of Eq. (44) is a simple Gaussian,

$$P(v,w) = \frac{C+g\tau_1}{\pi\Delta}\sqrt{(g+g_1)C/\tau_1}\exp\left\{-\frac{C+g\tau_1}{\Delta}\left[(g+g_1)\times\left(w-\frac{I_0}{g+g_1}\right)^2 + \frac{C}{\tau_1}(w-v)^2\right]\right\}. \tag{47}$$

Finding the solution to Eq. (44) with the threshold and reinjection boundary conditions is less easy. In the usual case of the IF model, the problem is similar to Kramer's well-known computation of the thermal escape from a one-dimensional potential well [26] and reduces to solving an ordinary differential equation. In the present two-dimensional nonpotential case, obtaining an exact solution to Eq. (44) appears to be a difficult task even in the stationary case. Instead of attempting this, a perturbative approach is developed here in the limit where the supplementary variable w evolves on a long time scale. This is a limit where subthreshold resonance is well developed. It is also relevant for subthreshold resonance in real cells [12] since most of them show preferred frequencies of a few Hertz [5–9,27–31]. When w evolves slowly as compared to the membrane potential v, it stays near the time-averaged potential $\langle v\rangle$ and the analysis of Eq. (44) can be reduced to that of an effective one-variable model. The analysis is first illustrated using a simple self-consistent approach in the zero-leak case ($g=0$). The general case is then dealt with in Sec. IV B using a direct expansion of the Fokker-Planck Eq. (44), which also provides a systematic means of computing higher perturbative orders as shown in the Appendix.

A. The zero-leak case

The GIF model of Eq. (6,7) with zero leak ($g=0$) is analyzed in this section in the limit $\tau_1 \to +\infty$.

1. Steady firing-rate

The steady firing-rate is considered first (with $I_{osc}(t)=0$). When $\tau_1 \to +\infty$, the relaxation of the supplementary variable w is driven by the time average of potential and in the steady state $w=\langle v\rangle$. The membrane potential dynamics reduces to the single Eq. (6) with w replaced by $\langle v\rangle$. The steady-state distribution of the membrane potential $P_s(v)$ thus obeys

$$(g_1\langle v\rangle - I_0)\partial_v P_s + \frac{\Delta}{2C}\partial_v^2 P_s = 0, \tag{48}$$

with the absorbing boundary condition at the threshold potential ($P_s(\theta)=0$) and the reinjection condition at the reset potential V_r. Multiplication of Eq. (48) by v and integration from $v=-\infty$ to the threshold $v=\theta$ directly relates the mean steady spike rate r_s and the average potential $\langle v\rangle$,

$$r_s = \frac{I_0 - g_1\langle v\rangle}{C(\theta - V_r)}, \tag{49}$$

where expression (46) for r_s and boundary condition (45) have been used to evaluate the boundary terms.

The full solution to Eq. (48) is also easily obtained and reads

$$P_s(v) = \frac{1}{\theta - V_r}\left\{1 - \exp\left[\frac{2C(g_1\langle v\rangle - I_0)}{\Delta}(\theta - v)\right]\right\}, \quad V_r < v < \theta$$

$$P_s(v) = \frac{1}{\theta - V_r}\left\{1 - \exp\left[\frac{2C(g_1\langle v\rangle - I_0)}{\Delta}(\theta - V_r)\right]\right\} \times \exp\left[\frac{2C(g_1\langle v\rangle - I_0)}{\Delta}(V_r - v)\right], \quad v < V_r. \tag{50}$$

The membrane potential distribution $P_s(v)$ depends on the average membrane potential $\langle v\rangle$, which remains to be determined. It is obtained in a self-consistent way by writing

$$\langle v\rangle = \int_{-\infty}^{+\infty} dv\, v\, P_s(v) = \frac{\theta + V_r}{2} + \frac{\Delta}{2C(g_1\langle v\rangle - I_0)}. \tag{51}$$

The last equality can be derived by integrating the exact expression (50) or again directly from Eq. (48), by multiplying it by v^2 and integrating from $v=-\infty$ to the threshold $v=\theta$. The simple self-consistent quadratic equation (51) has two roots, one larger and one smaller than I_0/g_1. Only the smaller one is compatible with a normalizable $P_s(v)$ [Eq. (50)] and with a positive spike rate [Eq. (49)]. One, therefore, obtains

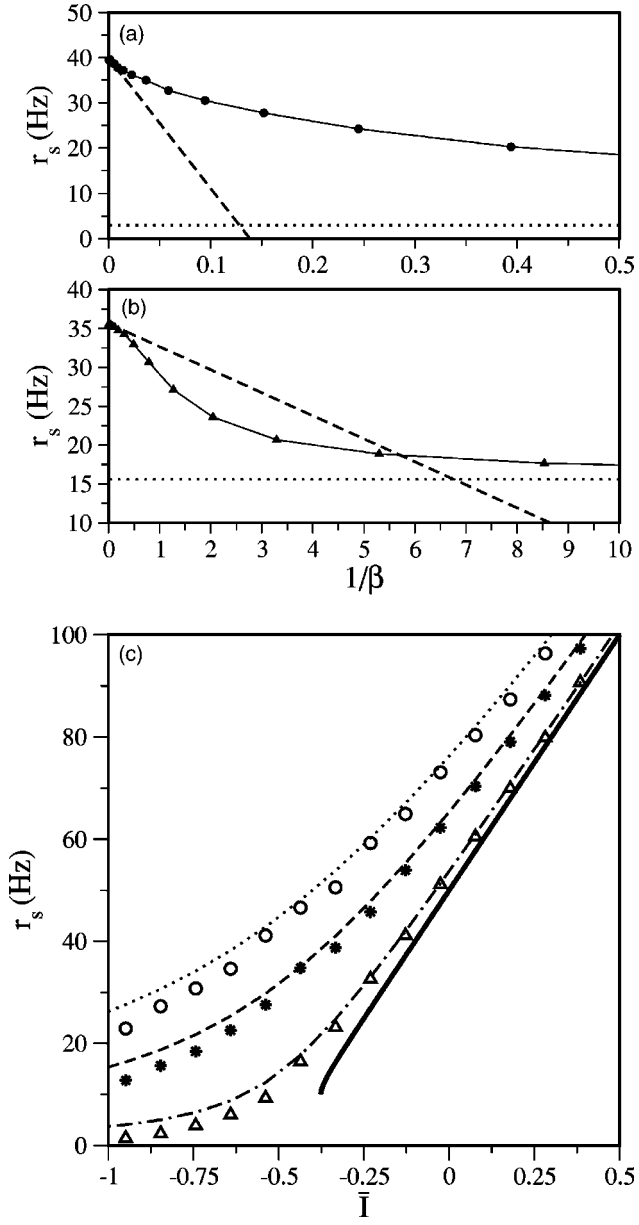

FIG. 6. Steady-state firing-rate for the zero-leak ($g=0$) GIF model with noisy inputs. The model parameters are $\theta=5$ mV, $V_r=0$ mV. Panels (a) and (b) show the variation of the firing rate with τ_1 when all other parameters are fixed ($\beta=\tau_1 g_1/C$). (a) $C/g_1=5$ ms, $I_0/g_1=-1.5$ mV, $\Delta/(Cg_1)=10(\mathrm{mV})^2$ (a high noise, low current case). (b) $C/g_1=10$ ms, $I_0/g_1=4$ mV, $\Delta/(Cg_1)=1(\mathrm{mV})^2$ (a low noise, high current case). The symbols are the results of direct simulations. The large τ_1 result of Eq. (53) and its first correction, Eq. (A14), are shown for comparison (dashed lines). The firing rate of a classic IF neuron with leak g_1 gives the small τ_1 approximation (dotted lines). (c) shows the firing rate as a function of the normalized injected current $\bar{I}=(I_0/g_1-\theta)/(\theta-Vr)$ for four noise levels. The symbols are the results of direct numerical simulation and the lines show the analytic result of Eq. (53). No noise, bold line; $\Delta/(Cg_1)=1(\mathrm{mV})^2$, triangles and dash-dotted line; $\Delta/(Cg_1)=5(\mathrm{mV})^2$, stars and dashed line; $\Delta/(Cg_1)=10(\mathrm{mV})^2$, circles and dotted line [$\tau_1=100$ ms and other model parameters as in (a)].

$$\langle v\rangle=\frac{1}{2g_1}\left\{I_0+g_1\frac{\theta+V_r}{2}-\sqrt{\left[I_0-g_1\frac{\theta+V_r}{2}\right]^2+\frac{2g_1\Delta}{C}}\right\}, \tag{52}$$

$$r_s=\frac{1}{2C(\theta-V_r)}\left\{\sqrt{\left[I_0-g_1\frac{\theta+V_r}{2}\right]^2+\frac{2g_1\Delta}{C}}+I_0-g_1\frac{\theta+V_r}{2}\right\}. \tag{53}$$

When $\Delta=0$, Eqs. (52) and (53) reduce to the simple noiseless expressions, $\langle v\rangle=I_0/g_1, r_s=0$ for $I_0<g_1(\theta+V_r)/2$ and $\langle v\rangle=(\theta+V_r)/2, r_s=[I_0-g_1(\theta+V_r)/2]/C(\theta-V_r)$ for $I_0/g_1>(\theta+V_r)/2$. One obtains again that the noiseless neuron has a periodically firing state when $I_0/g_1>(\theta+V_r)/2$, namely, for a smaller injected current than that which is required to bring its resting potential above the threshold (i.e., $I_0/g_1>\theta$). Moreover, for $\tau_1\to+\infty$, Eq. (53) shows that as soon as this periodic firing regime exists, it is selected by an infinitesimal noise.[2]

As shown in Fig. 6, results of direct simulations of the stochastic GIF model (6,7) tend toward the limiting values (52) and (53) when τ_1 increases. Higher order corrections to these lowest order estimates are obtained in the Appendix and are also plotted in Fig. 6.

2. Spike rate modulation by a small oscillatory current: Direct linearization

When the neuron is submitted to an additional small oscillatory current injection, $[I_{osc}(t)=\hat{I}/2\exp(i\omega t)+\text{c.c.}]$ in Eq. (44), its spike rate acquires a small modulation at the forcing frequency $r(t)=r_s+1/2[\hat{I}\hat{r}\exp(i\omega t)+\text{c.c.}]$. The aim here is to compute this modulation and to determine whether and under which conditions it displays a peak at the subthreshold resonance frequency. We first proceed straightforwardly and obtain the result for a fixed driving frequency ω in the limit $\tau_1\to+\infty$. It is then shown that the procedure needs some refinement to capture the subthreshold resonance for $\omega\sim\sqrt{g_1/\tau_1 C}$.

As discussed above, when $\tau_1\to+\infty$, the relaxation of the supplementary variable w is driven by the time average of the potential $w=\langle v\rangle$ and Eq. (6) reduces to the single-variable Fokker-Planck equation for the potential distribution,

$$\partial_t P=\frac{1}{C}[g_1\langle v\rangle-I_0-I_{osc}(t)]\partial_v P+\frac{\Delta}{2C^2}\partial_v^2 P. \tag{54}$$

The modulation due to the small oscillatory current $I_{osc}(t)$ is obtained by linearizing Eq. (54) around the steady-state so-

[2]For finite τ_1, this is presumably not the case. Determining in which part of the coexistence interval, the quiescent or the periodically firing regime is preferred in the low noise limit, would require computing and comparing the escape actions of these two attractors [37].

lution, seeking a probability distribution that has a small oscillating component at the injected current frequency $P(v,t)=P_s(v)+1/2[\hat{I}\hat{P}(v)\exp(i\omega t)+\text{c.c.}]+\cdots$. The modulation amplitude $\hat{P}(v)$ obeys

$$-i\omega\hat{P}+\frac{1}{C}(g_1\langle v\rangle-I_0)\partial_v\hat{P}]+\frac{\Delta}{2C^2}\partial_v^2\hat{P}=\frac{1}{C}\partial_v P_s. \tag{55}$$

The solution to Eq. (55) is easily obtained. First, comparison with the steady-state Eq. (48) provides a particular solution to the linear inhomogeneous Eq. (55) equal to $i\partial_v P_s/(C\omega)$. Second, in the present zero-leak case, the linear Eq. (55) has constant coefficients and its solution is therefore simply obtained as a superposition of exponentials $\exp(\lambda_\pm v)$ with

$$\lambda_\pm=\frac{C}{\Delta}[I_0-g_1\langle v\rangle\pm\sqrt{(g_1\langle v\rangle-I_0)^2+2i\Delta\omega}],\quad \mathrm{Re}(\lambda_\pm)\gtrless 0. \tag{56}$$

Taking into account the boundary conditions (45) and matching the function expressions in the two intervals $v<V_r, V_r<v<\theta$, one obtains

$$\hat{P}(v)=\frac{i}{\omega}\left\{\frac{2Cr_s}{\Delta}\exp[\lambda_+(v-\theta)]+\frac{1}{C}\partial_v P_s\right\},\ V_r<v<\theta$$

$$\hat{P}(v)=\frac{i}{\omega}\left\{\frac{2Cr_s}{\Delta}\{-1+\exp[\lambda_+(V_r-\theta)]\}\exp[\lambda_+(v-V_r)]+\frac{1}{C}\partial_v P_s\right\},\ v<V_r. \tag{57}$$

The corresponding spike rate modulation $1/2[\hat{r}^{IF}\hat{I}\exp(i\omega t)+\text{c.c.}]$ and mean voltage amplitude are simply

$$\hat{r}^{IF}=-i\frac{C(\theta-V_r)}{\Delta}\frac{r_s^2}{\omega}\left[\sqrt{1+2\,i\frac{\Delta\omega}{C^2(\theta-V_r)^2r_s^2}}-1\right], \tag{58}$$

$$\begin{aligned}\hat{v}_1^{IF}&=\int_{-\infty}^{\theta}dv\,v\,\hat{P}(v)\\&=\frac{i}{\omega}\left[(\theta-V_r)\hat{r}^{IF}-\frac{1}{C}\right]\\&=\left\{\frac{C(\theta-V_r)^2}{\Delta}\frac{r_s^2}{\omega^2}\left[\sqrt{1+2\,i\frac{\Delta\omega}{C^2(\theta-V_r)^2r_s^2}}-1\right]-\frac{i}{C\omega}\right\}.\end{aligned} \tag{59}$$

The superscript IF has been added to emphasize that the results are identical to what would have been obtained for a simple zero-leak IF model with injected current $[I_0-g_1\langle v\rangle=C(\theta-V_r)r_s]$. Therefore, modulation $\hat{r}^{IF}(\omega)$ is a monotonically decreasing function of frequency ω and does not display any sign of the subthreshold resonance, as shown in Fig. 7.

It can be noted that the deterministic peak at the firing-rate frequency, which exists for small noise for any finite τ_1 [Eq. (43)], is also missed by the lowest-order $\tau_1=\infty$ approximation. This is peculiar to the $g=0$ case and comes from the fact that the firing-rate resonance curve of the allied zero-leak IF model itself is special in not having a peak at the firing-rate frequency [22] as recalled previously.

The characteristic frequency r_s/K appears in Eq. (58), where K denotes the dimensionless ratio

$$K=\frac{\Delta}{2C^2(\theta-V_r)^2r_s}. \tag{60}$$

For further use below, we note the spike rate and mean voltage expansions for frequencies small compared to r_s/K,

$$\hat{r}^{IF}=\frac{1}{C(\theta-V_r)}\left[1-iK\frac{\omega}{r_s}-2\left(K\frac{\omega}{r_s}\right)^2+\cdots\right],$$

$$\hat{v}_1^{IF}=\frac{K}{Cr_s}\left[1-i2K\frac{\omega}{r_s}+\cdots\right]. \tag{61}$$

The corresponding expansions in the opposite frequency range $\omega\gg r_s/K$ read

$$\hat{r}^{IF}=\frac{e^{-i\pi/4}}{C(\theta-V_r)}\sqrt{\frac{r_s}{\omega K}}+\cdots,$$

$$\hat{v}_1^{IF}=\frac{1}{C\omega}\left(-i+e^{i\pi/4}\sqrt{\frac{r_s}{\omega K}}+\cdots\right). \tag{62}$$

3. Spike rate modulation by a small oscillatory current: The low frequency regime

Considering the zero frequency limit provides a hint that the perturbative result of Eq. (58) does, however, not entirely describe the spike rate modulation dependence on frequency. On one hand, when $\omega\to 0$, Eq. (58) gives the limiting behavior

$$\lim_{\omega\to 0}\hat{r}^{IF}=\frac{1}{C(\theta-V_r)}. \tag{63}$$

On the other hand, the spike rate modulation induced by a very slowly changing injected current should be given by the variation of the steady-state firing-rate with a change in the *constant* current from I_0 to $I_0+I_{osc}(t)$,

$$\lim_{\omega\to 0}\hat{r}=\frac{dr_s}{dI_0}=\frac{1}{C(\theta-V_r)}\left(1-g_1\frac{d\langle v\rangle}{dI_0}\right) \tag{64}$$

$$=\frac{1}{2C(\theta-V_r)}\left(1+\frac{I_0-g_1(\theta+V_r)/2}{\sqrt{[I_0-g_1(\theta+V_r)/2]^2+2g_1\Delta/C}}\right), \tag{65}$$

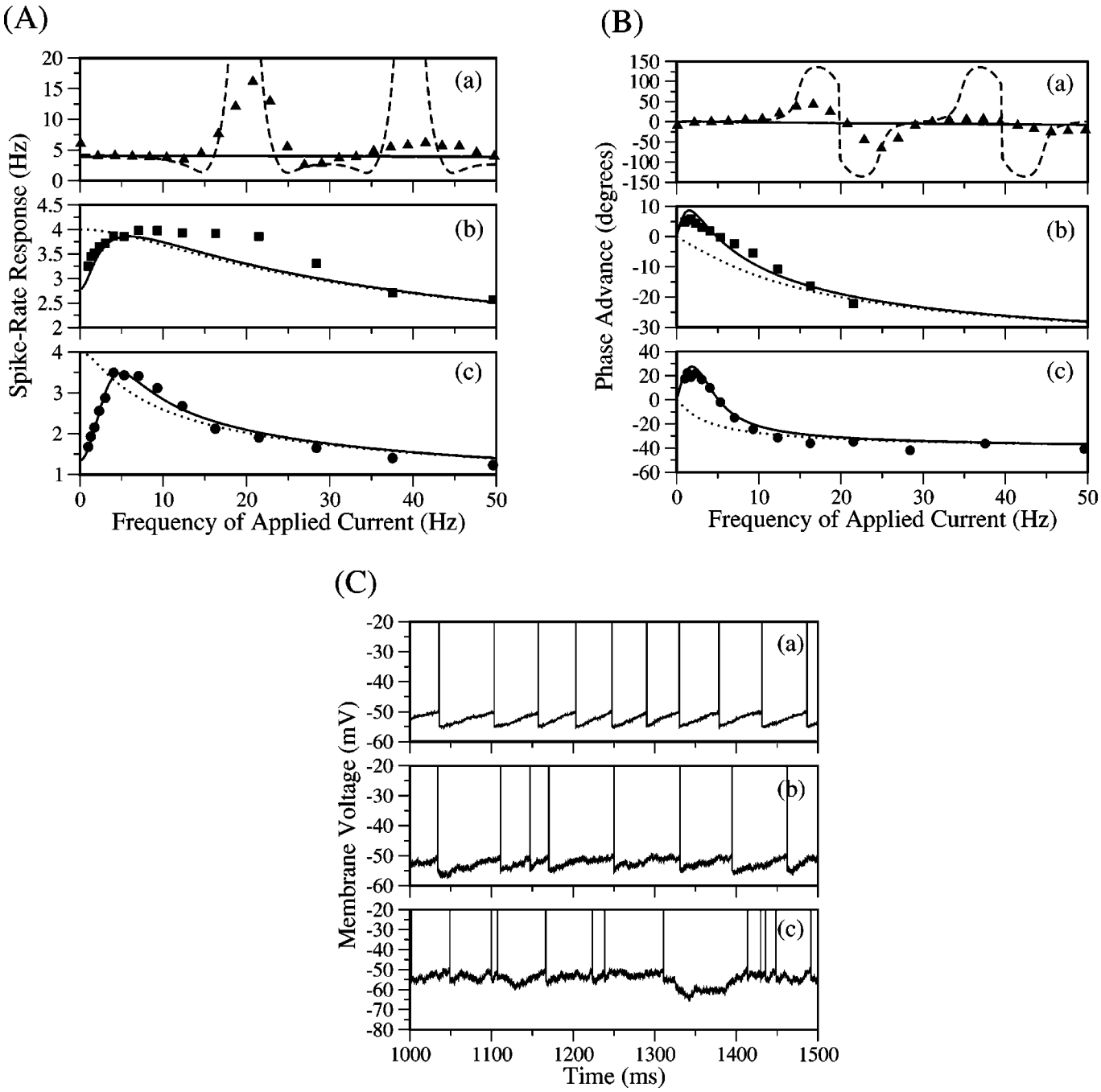

FIG. 7. Firing-rate resonance curves in the zero-leak case. (A) Modulus of the firing-rate modulation $\hat{I}\hat{r}_1(\omega)$. (B) Phase of the firing-rate modulation. The triangles are the results of direct numerical simulation; the lines correspond to the analytic formula (73). (C) Samples of membrane potential traces. In (A) and (B), symbols are the results of direct numerical simulations, the dotted lines show the large τ_1 analytic expression (58), and the thick lines show the refined expression (73). The zero-noise result (42) is also shown for comparison (dashed lines). Three different noise and injected current conditions are shown. $\hat{I}=0.02$ with (a) $\Delta=0.01$, $I_0=0.35$; (b) $\Delta=0.1$, $I_0=0.31$; and (c) $\Delta=0.5$, $I_0=0.14$. The other model parameters are $C=1$, $g_1=0.1$, $\tau_1=100$ (units as in Fig. 6). As noise increases, the peak shifts from the firing-rate frequency around 20 Hz in (a) to the subthreshold resonance frequency of about 5 Hz in (c).

where the last two equalities follow from Eqs. (49) and (58). Since the average membrane potential $\langle v \rangle$ depends on the injected current I_0, results (63) and (64) are different. The origin of the discrepancy is that they correspond to different limiting procedures (see Fig. 7). The perturbative result (63) is obtained by first computing the limit of $\hat{r}(\omega)$ when $\tau_1 \to +\infty$ at a fixed nonzero frequency and then taking the limit $\omega \to 0$. Contrary to this, Eq. (64) corresponds to first setting

$\omega=0$ and then evaluating the limit of $\hat{r}(0)$ when $\tau_1\to+\infty$. The two results differ because $\hat{r}(\omega)$ has a rapid variation near $\omega=0$ in a small frequency range that tends to zero when $\tau_1\to+\infty$, as a consequence of the fact that the subthreshold resonance $\sim\sqrt{g_1/\tau_1 C}$ also tends to zero in this limit.

This being noted, the previous calculation can be refined so that it correctly interpolates between the two frequency regimes $\omega\ll\sqrt{g_1/\tau_1 C}$ and $\omega\gg\sqrt{g_1/\tau_1 C}$. A simple approach is presented here. A more systematic way of proceeding is presented in Sec. IV B.

As previously, we consider the limit $\tau_1\gg 1$ with a weak driving term but at frequency ω that is arbitrarily slow. In this case, the potential v has short time fluctuations but also slow oscillations at frequency ω. Averaging on a time that is long for the random fluctuations but short compared to the period $2\pi/\omega$ of the oscillation gives

$$\langle v\rangle = v_0 + \tfrac{1}{2}[\hat{I}\hat{v}_1\exp(i\omega t)+\text{c.c.}]. \tag{66}$$

Integration of Eq. (7) provides the corresponding expression for w,

$$w(t) = v_0 + \frac{1}{2}\left[\frac{\hat{I}\hat{v}_1}{1+i\omega\tau_1}\exp(i\omega t)+\text{c.c.}\right]. \tag{67}$$

Since w is no longer a fluctuating variable, Eq. (6) reduces as before to a single-variable Fokker-Planck equation

$$\partial_t P = \frac{1}{C}[g_1 w(t) - I_0 - I_{osc}(t)]\partial_v P + \frac{\Delta}{2C^2}\partial_v^2 P, \tag{68}$$

where $w(t)$ is given by Eq. (67). Expanding $P(v,t)$, as above, under the form $P(v,t)=P_s(v)+1/2[\hat{I}\hat{P}(v)\exp(i\omega t)+\text{c.c.}]+\cdots$, gives a modified equation for $\hat{P}$,

$$-i\omega\hat{P} + \frac{1}{C}(g_1\langle v\rangle - I_0)\partial_v\hat{P} + \frac{\Delta}{2C^2}\partial_v^2\hat{P} = \frac{1}{C}\left[1-\frac{g_1\hat{v}_1}{1+i\omega\tau_1}\right]\partial_v P_s. \tag{69}$$

Equation (69) is identical to Eq. (55) except that the inhomogeneous rhs of these two linear equations differ by a constant proportionality factor. The solution to Eq. (69) is therefore obtained by multiplying the solution to Eq. (55) by the same factor (this is also consistent with the boundary conditions at threshold and reset). In particular, this gives the two relations

$$\hat{v}_1 = \int_{-\infty}^{\theta} dv\, v\hat{P}(v) = \left[1-\frac{g_1\hat{v}_1}{1+i\omega\tau_1}\right]\hat{v}_1^{IF}, \tag{70}$$

$$\hat{r} = -\frac{\Delta}{2C^2}\partial_v\hat{P}(v)|_\theta = \left[1-\frac{g_1\hat{v}_1}{1+i\omega\tau_1}\right]\hat{r}^{IF}, \tag{71}$$

where $\hat{v}_1^{IF}$ is the previously computed oscillation amplitude [Eq. (59)]. Equation (70) self-consistently determines the amplitude of the average potential oscillations

$$\hat{v}_1 = \frac{1+i\omega\tau_1}{1+i\omega\tau_1+g_1\hat{v}_1^{IF}}\hat{v}_1^{IF}. \tag{72}$$

Together with Eq. (72), this also completes the determination of the spike rate modulation amplitude (to lowest order)

$$\hat{r} = \frac{1+i\omega\tau_1}{1+i\omega\tau_1+g_1\hat{v}_1^{IF}}\hat{r}^{IF} = \frac{1+i\omega\tau_1}{1+i\omega\tau_1+g_1[1-(\theta-V_r)\hat{r}^{IF}]/(iC\omega)}\hat{r}^{IF}, \tag{73}$$

where Eq. (59) has been used to obtain the second equality. Equation (73) gives that the firing-rate modulation amplitude is maximal at a nonzero frequency ω_{pfr}. It is compared with the results of direct numerical simulations in Fig. 7. The analytic long τ_1 result misses the resonance at the firing frequency that is captured by the noiseless expression, Eq. (42). For low noise, this resonance is dominant and the approximation poorly describes the numerics in this frequency range. For higher noise, the resonance at the firing frequency disappears and the dominant modulation lies around the subthreshold resonance frequency. Equation (73) then describes the numerical data quite well (see Fig. 7 lower panels).

The frequency ω_{pfr} corresponding to the maximal spike rate modulation can be estimated simply when the subthreshold frequency is much smaller than the characteristic frequency r_s/K (which approximately corresponds to the parameters chosen in Fig. 7) or in the opposite case when it is much larger. In the first case, we consider the frequency range $1/\tau_1\ll\omega\ll r_s/K$, where the different terms of Eq. (73) can be expanded as follows [Eq. (61)]:

$$|\hat{r}|^2 = |\hat{r}^{IF}(0)|^2\left[1+\frac{1}{\omega^2\tau_1^2}\right]\times\left[1+\frac{4K^2g_1}{r_s^2\tau_1 C}-\frac{(1+Kg_1/r_sC)^2}{\omega^2\tau_1^2}+\cdots\right]\times\left[1-3\left(K\frac{\omega}{r_s}\right)^2+\cdots\right] \tag{74}$$

$$= |\hat{r}^{IF}(0)|^2\left[1+\frac{4K^2g_1}{r_s^2\tau_1 C}-\frac{(2r_sC/g_1+K)K}{\omega^2\tau_1^2}\left(\frac{g_1}{Cr_s}\right)^2 - 3\left(K\frac{\omega}{r_s}\right)^2+\cdots\right]. \tag{75}$$

This gives the peak frequency

$$\omega_{pfr}\simeq\left[\frac{2r_sC/g_1+K}{3K}\right]^{1/4}\sqrt{\frac{g_1}{\tau_1 C}}. \tag{76}$$

Therefore, apart from a numerical factor, the peak modulation of the spike rate coincides with the resonant subthreshold frequency $\sqrt{g_1/\tau_1 C}$. In the limit considered here, the spike rate resonance is, however, broader than the subthreshold one. As shown by Eq. (75), its width is comparable to ω_{pfr} while the subthreshold resonance peak is much sharper with a width $\sim 1/\tau_1$. The phase of $\hat{r}$ can be similarly analyzed. In the frequency range $1/\tau_1 \ll \omega \ll r_s/K$, the expansion of $\hat{r}$ reads

$$\hat{r}(\omega)=\frac{1}{C(\theta-V_r)}\left[1+i\frac{Kg_1}{r_s C}\left(\frac{1}{\omega\tau_1}-\omega C/g_1\right)+\cdots\right]. \tag{77}$$

So, the phase of $\hat{r}$ decreases monotonically in this frequency range and *vanishes* at the resonant subthreshold frequency $\omega_p \sim \sqrt{g_1/\tau_1 C}$. The maximum of the phase stands at a lower frequency, which is only determined, for $\tau_1 \to +\infty$, by the prefactor of $\hat{r}^{IF}$ in Eq. (73). In the low frequency range $\omega \sim 1/\tau_1$, the phase of $\hat{r}^{IF}$ coincides with the phase of $[1+i\omega\tau_1]/[1+i\omega\tau_1+g_1\hat{v}_1^{IF}(\omega=0)]$. Its maximum stands at

$$\omega=[1+g_1\hat{v}_1^{IF}(\omega=0)]^{1/2}\frac{1}{\tau_1}=\left[1+\frac{g_1 K}{C r_s}\right]^{1/2}\frac{1}{\tau_1}. \tag{78}$$

The opposite case when the subthreshold frequency ω_p is larger than the characteristic frequency r_s/K can be analyzed in a similar way. For $\omega \sim \omega_p$, the firing modulation can be approximately written as [Eq. (62)]

$$\hat{r}=\frac{e^{-i\pi/4}}{C(\theta-V_r)}\sqrt{\frac{r_s}{\omega K}}\frac{1+i\omega\tau_1}{1+i(\omega\tau_1-g_1/C\omega)}. \tag{79}$$

It is maximal at the resonant subthreshold frequency. This is also the frequency where the phase of $\hat{r}(\omega)$ vanishes. The phase maximum stands at the smaller frequency $\omega_p/\sqrt{3}$.

B. The general two-variable case

It is conceptually not more difficult to analyze the general two-variable GIF model case than the previous $g=0$ case. We restrict ourselves to $g>0$ so that the model is stable when $\tau_1 \gg \tau$ (i.e., so that $\alpha=\tau_1 g/C>-1$ in this limit). The computation, however, involves more complicated functions and less explicit expressions. Instead of simply repeating the previous analysis, here the appropriate generalized expressions are obtained from a direct expansion of the Fokker-Planck equation (44) in the large τ_1 limit. We find it convenient to introduce $\sigma=\sqrt{\Delta/Cg}$, which measures the amplitude of the fluctuations in voltage units, the time constant $\tau=C/g$, and the conductance ratio $\gamma=g_1/g$. With these notations, the limit considered is that of large $\beta=\tau_1 g_1/C$ at fixed σ and γ.

1. Steady firing rate

With a steady noisy injected current [i.e., $I_{osc}(t)=0$], the membrane potential distribution obeys the time-independent version of the Fokker-Planck equation (44). Anticipating that w does not fluctuate in the limit $\beta \to +\infty$, we introduce the new variable z with

$$w=\overline{w}+z\sigma\beta^a, \tag{80}$$

where the constant value $\overline{w}$ and the power $a<0$ remain to be determined. With this new variable, the steady-state probability distribution P_s obeys

$$\begin{aligned}\partial_v[(gv+g_1\overline{w}-I_0)P_s]+\frac{\sigma^2}{2\tau}\partial_v^2 P \\ =-g_1\left\{\sigma\beta^a z\partial_v P_s+\sigma^{-1}\beta^{-a-1}\partial_z[(\overline{w}-v)P_s]\right. \\ \left.+\frac{1}{\beta}\partial_z[zP_s]\right\}.\end{aligned} \tag{81}$$

The first two subdominant terms on the rhs of Eq. (81) are of same order when $\beta^a \sim \beta^{-a-1}$, i.e., for $a=-1/2$ that we choose. In order to simplify further expressions, we find it convenient to also replace v by the dimensionless variable y with

$$y=\frac{gv+g_1\overline{w}-I_0}{g\sigma}. \tag{82}$$

In these notations, the time-independent Fokker-Planck equation finally reads

$$\begin{aligned}\frac{1}{2}\frac{\partial^2 P_s}{\partial y^2}+\frac{\partial}{\partial y}(yP_s)=-\gamma\left\{\frac{1}{\sqrt{\beta}}\left(z\frac{\partial P_s}{\partial y}+(\overline{y}-y)\frac{\partial P_s}{\partial z}\right)\right. \\ \left.+\frac{1}{\beta}\frac{\partial}{\partial z}(zP_s)\right\},\end{aligned} \tag{83}$$

where $\gamma=g_1/g$ and we have defined $\overline{y}=[(g+g_1)\overline{w}-I_0]/(g\sigma)$. With variables y and z, the boundary conditions are imposed at the threshold y_θ and at the reset potential y_r,

$$y_\theta=\frac{1}{g\sigma}(g\,\theta+g_1\overline{w}-I_0),\quad y_r=\frac{1}{g\sigma}(g\,V_r+g_1\overline{w}-I_0). \tag{84}$$

The boundary conditions read

$$\begin{aligned}P(y_\theta,z)=[P(y,z)]_{y_r^-}^{y_r^+}=0, \\ \frac{1}{2}\frac{\partial P}{\partial y}(y_\theta,z)=\frac{1}{2}\left[\frac{\partial P}{\partial y}(y,z)\right]_{y_r^-}^{y_r^+}=-r(z),\end{aligned} \tag{85}$$

where the square brackets denotes the discontinuity of the bracketed quantity $[f(y)]_{y_r^-}^{y_r^+}=\lim_{\epsilon\to 0}\{f(y_r+\epsilon)-f(y_r-\epsilon)\}$. The firing-rate is equal to the total rate of threshold crossing.

With the new variables and the normalization of P chosen as $\int_{-\infty}^{y_\theta} dy \int_{-\infty}^{+\infty} dz P(y,z) = 1$, it reads

$$r = \frac{1}{\tau} \int_{-\infty}^{+\infty} dz\, r(z). \tag{86}$$

When β is large, the solution to Eq. (83) can be obtained by series expansion,

$$P_s(y,z) = P_0(y,z) + \beta^{-1/2} P_1(y,z) + \beta^{-1} P_2(y,z) + \cdots,$$

$$r_s(z) = r_0(z) + \beta^{-1/2} r_1(z) + \beta^{-1} r_2(z) + \cdots. \tag{87}$$

The zeroth-order solution is obtained by neglecting the rhs of Eq. (83),

$$P_0(y,z) = 2 r_0(z) Q_0(y), \tag{88}$$

$$Q_0(y) = e^{-y^2} \int_y^{y_\theta} e^{u^2} \Theta(u - y_r) du, \tag{89}$$

where Θ is the usual Heaviside function, $\Theta(u) = 1$ for $x \geqslant 0$ and 0 otherwise. It is identical to the steady-state probability distribution for the usual leaky integrate-and-fire model (see, e.g., Ref. [17]) except that the prefactor $r_0(z)$ is a function of the supplementary variable z instead of a constant and remains to be obtained as well as the bounds y_θ and y_r that depend on the unknown $\overline{w}$ [see Eqs. (80) and (84)]. These unknowns are determined by solvability conditions on higher-order equations.

The first-order correction $P_1(y,z)$ obeys

$$\frac{1}{2} \frac{\partial^2 P_1}{\partial y^2} + \frac{\partial}{\partial y}(y P_1) = -\gamma \left(z \frac{\partial P_0}{\partial y} + (\overline{y} - y) \frac{\partial P_0}{\partial z} \right). \tag{90}$$

The integral over y on the lhs of Eq. (90) from $y = -\infty$ to $y = y_\theta$ is seen to vanish after using boundary conditions (85). Therefore, this needs to be also true for the rhs of Eq. (90) if the equation is to be solvable. That is,

$$\int_{-\infty}^{y_\theta} dy (\overline{y} - y) Q_0(y) = 0. \tag{91}$$

This solvability condition determines $\overline{w}$ (and, therefore, y_θ, y_r and $\overline{y}$). It is equivalent to the previous self-consistent equation (51), which was obtained on a more intuitive basis.

Once $\overline{w}$ is determined, the normalization condition gives the steady-state rate to lowest order in $1/\beta$,

$$\frac{1}{r_0 \tau} = 2 \int_{-\infty}^{y_\theta} Q_0(y) = \int_0^{+\infty} du e^{-u^2} \frac{\exp(2 y_\theta u) - \exp(2 y_r u)}{u}. \tag{92}$$

When condition (91) is satisfied, Eq. (90) can be solved without difficulty. As can be seen from the rhs of Eq. (90) and explicitly given in the Appendix, the resulting $P_1(y,z)$ is obtained as a linear combination of $r_0'(z)$ and $z r_0(z)$ multiplied by determined functions of y. The solvability condition on P_1 at second order, analogous to Eq. (91), imposes that $r_0'(z)$ is proportional to $z r_0(z)$ and shows that $r_0(z)$ is a Gaussian. The explicit expression of $\langle z^2 \rangle_0$ as well as the first nontrivial correction to r_0 are determined in the Appendix [see Eqs. (A28)–(A30)]. A comparison between direct numerical simulation results and the perturbative estimates of the steady-state rate is provided in Fig. 8. The large τ_1 result (92) is seen to describe quite accurately the numerical results already for $\tau_1/\tau = 5$.

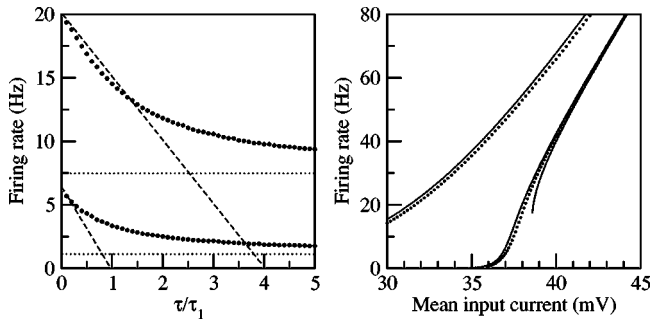

FIG. 8. Steady-state firing rate r_0 for a leaky GIF model with $\gamma = 1$, $\tau = C/g = 20$ ms, $\theta = 20$ mV, and $V_r = 14$ mV. Left panel: dependence of r_0 on the ratio of time constants, for $\sigma = 1$ mV and $I_0/g = 37$ mV (curves at low firing rates) and $I_0/g = 38$ mV (curves at higher firing rates). Circles, numerical simulations; dashed line, analytical expression for the firing rate including the first correction in the large τ_1 expansion, Eqs. (92) and (A31); dotted line, the analytical expression for the firing rate in the limit $\tau_1 = 0$, which is that of a usual IF model with a leak equal to $g + g_1$. Right panel: r_0 as a function of the injected current I_0/g for $\tau_1 = 100$ ms for zero noise, $\sigma = 1$ mV and $\sigma = 5$ mV. Solid lines, zero-order analytic calculations; circles, simulations.

2. Spike rate modulation: Direct linearization

In order to obtain the instantaneous spike rate modulation induced by a small oscillatory current ($I_{osc}(t) = 1/2 \hat{I} \exp(i\omega t) + \text{c.c.}$), we consider the direct linearization of the time-dependent Fokker-Planck equation (44) around the steady-state distribution.

In variables y,z, Eq. (44) reads

$$-\tau \partial_t P + \frac{1}{2} \frac{\partial^2 P}{\partial y^2} + \frac{\partial}{\partial y}(y P) = -\gamma \left\{ \frac{1}{\sqrt{\beta}} \left(z \frac{\partial P}{\partial y} + (\overline{y} - y) \frac{\partial P}{\partial z} \right) + \frac{1}{\beta} \frac{\partial}{\partial z}(z P) \right\} + \frac{I_{osc}(t)}{g\sigma} \partial_y P, \tag{93}$$

with boundary conditions (85) [with a time-dependent $r(z,t)$]. $P(y,z,t)$ and $r(z,t)$ are sought in the form $P(y,z,t) = P^s(y,z) + (2g\sigma)^{-1} [\hat{I} \hat{P}(y,z) \exp(i\omega t) + \text{c.c.}]$, $r(z,t) = r_s(z) + (2g\sigma)^{-1} [\hat{I} \hat{r}(z,\omega) \exp(i\omega t) + \text{c.c.}]$. The firing rate [Eq. (86)] and its modulation are obtained by integration over z (and division by τ) and are written as

$$r(t)=r_s+(2g\sigma)^{-1}[\hat{I}\,\hat{r}(\omega)\exp(i\omega t)+\text{c.c.}]. \quad (94)$$

Note that the normalization of the current in this section makes the normalization of $\hat{r}(\omega)$ differ by a factor $g\sigma$ from the normalization in Eq. (9). Modulation $\hat{P}$ obeys at lowest order in $1/\sqrt{\beta}$,

$$-i\tau\omega\hat{P}_0+\frac{1}{2}\frac{\partial^2\hat{P}_0}{\partial y^2}+\frac{\partial}{\partial y}(y\hat{P}_0)=\partial_y P_0. \quad (95)$$

At this order, the z dependence of $\hat{P}_0$ factors out and it can be written as

$$\hat{P}_0=2r_0(z)\hat{Q}_0^{IF}, \quad (96)$$

where $\hat{Q}_0^{IF}$ is identical to the response of a classic IF neuron under oscillatory drive. The function $\hat{Q}_0^{IF}$ can be written [17,25] as a linear combination of a particular solution to Eq. (95) plus two independent solutions ϕ_1 and ϕ_2 of the allied homogeneous equation. The particular solution of Eq. (95), $\partial_y Q_0/[1+i\omega\tau]$, is obtained by differentiating the steady-state equation to lowest order [i.e., Eq. (83) with rhs equal to zero] with respect to y. Introducing Kummer's function $M(a,b,x)$ [32], functions $\phi_1(y)$ and $\phi_2(y)$ can be taken as independent linear combinations of the confluent hypergeometric functions $M[(1-i\omega\tau)/2,1/2,-y^2]$ and $yM[1-i\omega\tau/2,3/2,-y^2]$. It is convenient to choose $\phi_2(y)$ proportional to the combination that has a fast decrease at $y=-\infty$,

$$\phi_2(y)=\frac{1}{\Gamma\left(\frac{1+i\omega\tau}{2}\right)}M\left(\frac{1-i\omega\tau}{2},\frac{1}{2},-y^2\right)+\frac{2y}{\Gamma\left(\frac{i\omega\tau}{2}\right)}M\left(1-i\frac{\omega\tau}{2},\frac{3}{2},-y^2\right). \quad (97)$$

This gives the zeroth-order estimate of $\hat{r}(\omega)$ [Eq. (94)],

$$\hat{Q}_0^{IF}(y)=-\frac{1}{1+i\omega\tau}\frac{dQ_0}{dy}+\begin{cases}\hat{\alpha}_0\phi_2(y), & y<y_r\\ \hat{\beta}_0\phi_1(y)+\hat{\gamma}_0\phi_2(y), & y>y_r.\end{cases} \quad (98)$$

The three boundary conditions (85) determine the three unknown coefficients $\hat{\alpha}_0(\omega)$, $\hat{\beta}_0(\omega)$, and $\hat{\gamma}_0(\omega)$ and give the firing-rate modulation

$$\hat{r}_0^{IF}(\omega)=\frac{r_0}{1+i\omega\tau}\left(\frac{[\phi_2'(y_\theta)+2y_\theta\phi_2(y_\theta)]\exp(y_\theta^2)-[\phi_2'(y_r)+2y_r\phi_2(y_r)]\exp(y_r^2)}{\phi_2(y_\theta)\exp(y_\theta^2)-\phi_2(y_r)\exp(y_r^2)}\right). \quad (99)$$

Again, we have added the superscript IF to emphasize that the rate modulation (99) is identical to the result for a classic IF model with an injected current $I_0-g_1\overline{w}$. For further use below, we also note that integration of Eq. (95) over y provides the identity

$$Y(\omega)\equiv 2\tau r_0\int_{-\infty}^{y_\theta}dy\,y\hat{Q}_0^{IF}=\frac{1-(y_\theta-y_r)\hat{r}_0^{IF}(\omega)\tau}{1+i\omega\tau}, \quad (100)$$

where function $Y(\omega)$ is defined by the first equality.

The obtained firing-rate modulation $\hat{r}_0^{IF}(\omega)$ is plotted and compared to the results of a direct numerical simulation of the GIF model in Fig. 9.

The agreement is rather good at high frequency but does not capture the resonance at low frequency. Moreover, as for the previous zero-leak case, the zero frequency limit of Eq. (99) does not correspond to the result obtained by varying the injected current in the steady-state rate (92). That is,

$$\hat{r}_0^{IF}(\omega=0)=2\tau r_0^2\left(e^{y_\theta^2}\int_{-\infty}^{y_\theta}e^{-u^2}du-e^{y_r^2}\int_{-\infty}^{y_r}e^{-u^2}du\right). \quad (101)$$

This differs from the expected formula for very slow oscillations, which should be given by the adiabatic oscillations of the steady-state rate. Namely, from Eq. (92) one obtains

$$\lim_{\omega\to 0}\widehat{r_0}(\omega)=g\sigma\frac{dr_0}{dI_0}=\hat{r}_0^{IF}(0)\left[1-g_1\frac{d\overline{w}}{dI_0}\right], \quad (102)$$

where $\overline{w}$ is determined by Eq. (91) and depends on I_0 because y_θ and y_r do. As before, the two formulas differ because the variation of $\overline{w}$ due to the injected current is overlooked in the direct linearization. The approach should therefore be refined at low frequency as shown in the following section.

3. Spike rate modulation: The low frequency regime

In the low frequency regime, the terms coming from time differentiation become small and comparable to the terms of first order in $1/\sqrt{\beta}$. Thus, the perturbation series has to be reordered.

The adiabatic result at $\omega=0$ lead us to anticipate that, for a slow oscillating current $I_{osc}(t)=1/2\,[\hat{I}\exp(i\omega t)+\text{c.c.}]$, w is peaked around a time-dependent oscillating value. This suggests a change of variables from w to z with

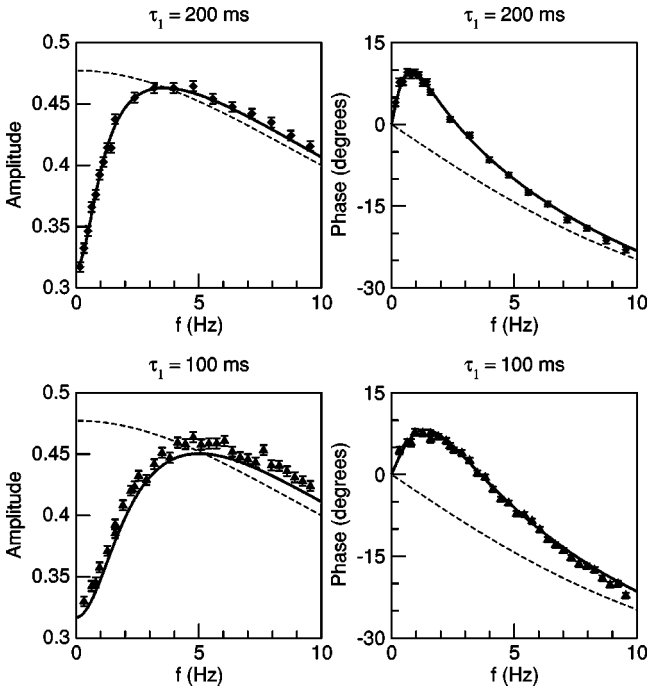

FIG. 9. Relative firing-rate modulation as a function of frequency $f=\omega/2\pi$ for the leaky GIF model. The amplitude (left) and phase (right) of $\hat{r}\hat{I}/(g\sigma r_s)$ are shown for two different values of τ_1 (indicated above each panel) in the strong noise regime. The peak of the amplitude stands around the subthreshold resonance frequency (about 3.5 Hz for the top panels and 5 Hz for the bottom panels). Parameters of the input: $I_0/g=29$ mV, $\sigma=5$ mV yielding a steady firing rate of about 12 Hz, $\gamma=1$. Other parameters are as in Fig. 8. Symbols, numerical simulations with $\hat{I}=0.05I_0$; thick line, analytical expression, Eq. (116); thin line, firing-rate modulation and phase of the IF neuron, Eq. (99). It can be noted that the linear approximation still gives a good fit to the data for a modulation of about 50%, as seen here.

$$w=\overline{w}+1/2[\hat{I}\,\hat{w}_1\exp(i\omega t)+\text{c.c.}]+z\sigma\beta^{-1/2}. \quad (103)$$

This transforms the Fokker-Planck equation (44) into

$$\begin{aligned}-\tau\partial_t P+\frac{1}{2}\frac{\partial^2 P}{\partial y^2}+\frac{\partial}{\partial y}(yP)&\\ =-\gamma\left\{\frac{1}{\sqrt{\beta}}\left(z\frac{\partial P}{\partial y}+(\overline{y}-y)\frac{\partial P}{\partial z}\right)+\frac{1}{\beta}\frac{\partial}{\partial z}(zP)\right\}&\\ +\frac{1}{2g\sigma}\left\{\left[(1-g_1\hat{w}_1)\partial_y P-\frac{1+i\omega\tau_1}{\sqrt{\beta}}g_1\hat{w}_1\partial_z P\right]\hat{I}\right.&\\ \left.\times\exp(i\omega t)+\text{c.c.}\right\},&\quad (104)\end{aligned}$$

where, as before, we have also introduced $y=[(g\upsilon+g_1\overline{w}-I_0]/(g\sigma)$ and defined the corresponding constant $\overline{y}=[(g+g_1)\overline{w}-I_0]/(g\sigma)$.

Again, the solution to (104) is sought of the form $P(y,z,t)=P_s(y,z)+(2g\sigma)^{-1}[\hat{I}\,\hat{P}(y,z)\exp(i\omega t)+\text{c.c.}]$. For low frequencies $\omega\sim 1/\sqrt{\tau\tau_1}$ (or smaller), the linear probability modulation obeys to lowest order in $1/\sqrt{\beta}$,

$$\frac{1}{2}\frac{\partial^2\hat{P}_0}{\partial y^2}+\frac{\partial}{\partial y}(y\hat{P}_0)=(1-g_1\hat{w}_1)\partial_y P_0. \quad (105)$$

Equation (105) only differs from the previously solved Eq. (95), in that it is evaluated at $\omega=0$ and that the rhs of the two equations differ by a constant proportionality factor. Therefore, one has

$$\hat{P}_0=2r_0(z)[1-g_1\hat{w}_1]\hat{Q}_0^{IF}(y;\omega=0), \quad (106)$$

$$\hat{r}_0=[1-g_1\hat{w}_1]\hat{r}_0^{IF}(\omega=0), \quad (107)$$

with

$$\begin{aligned}\hat{Q}_0^{IF}(y;\omega=0)=-\frac{\partial Q_0}{\partial y}+\frac{\hat{r}_0^{IF}(\omega=0)}{r_0}Q_0(y)+\exp(-y^2)&\\ \times[-\exp(y_\theta^2)+\Theta(y_r-y)\exp(y_r^2)],&\quad (108)\end{aligned}$$

where r_0 and $\hat{r}_0(\omega=0)$ are given by Eqs. (92) and (101). Formula (108) can be obtained by taking the limit $\omega\to 0$ of general expression (98) or more simply by directly solving Eq. (95) with $\omega=0$. In this case, the normalization condition to the solution of the homogeneous equation can be obtained by imposing the condition

$$\int_{-\infty}^{y_\theta}dy\,\hat{Q}_0^{IF}(y)=0, \quad (109)$$

which directly follows from Eq. (95) for $\omega\neq 0$.

The unknown constant $\hat{w}_1$ is determined by a solvability condition at next order. The $1/\sqrt{\beta}$ correction $\hat{P}_1$ to $\hat{P}_0$ obeys

$$\begin{aligned}\frac{1}{2}\frac{\partial^2\hat{P}_1}{\partial y^2}+\frac{\partial}{\partial y}(y\hat{P}_1)=-\gamma\left[z\frac{\partial\hat{P}_0}{\partial y}+(\overline{y}-y)\frac{\partial\hat{P}_0}{\partial z}\right]&\\ +(1-g_1\hat{w}_1)\partial_y P_1-(1+i\omega\tau_1)&\\ \times(g_1\hat{w}_1)\partial_z P_0+i\omega\tau\sqrt{\beta}\hat{P}_0. &\quad (110)\end{aligned}$$

The solvability condition, obtained by integrating Eq. (110) over y together with Eq. (106) and (109), reads

$$\int_{-\infty}^{y_\theta}dy\{\gamma(\overline{y}-y)\hat{P}_0+(1+i\omega\tau_1)g_1\hat{w}_1P_0\}=0. \quad (111)$$

With the previous expressions (106) and (108), Eq. (111) is found to be equivalent to the following self-consistent equation for $\hat{w}_1$:

$$g_1\hat{w}_1=\gamma\frac{(1-g_1\hat{w}_1)}{1+i\omega\tau_1}2\tau r_0\int_{-\infty}^{y_\theta}dy\,y\hat{Q}_0^{IF}(y,\omega=0). \quad (112)$$

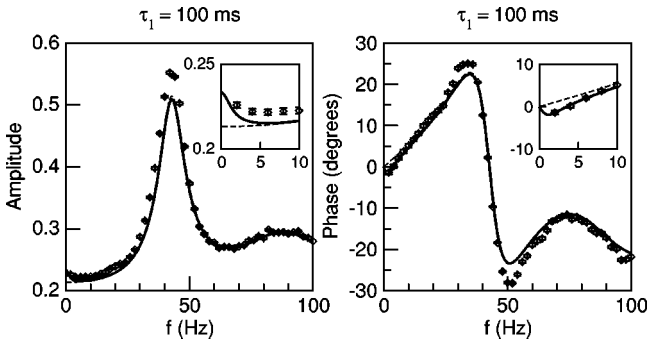

FIG. 10. Firing-rate resonance curve in the low noise regime. Same parameters as in Fig. 9, except that $I_0/g=40$ mV, $\sigma=1$ mV, giving a background firing rate of about 42 Hz. Simulations are performed with $I_1=0.025I_0$. The symbols correspond to the results of direct numerical simulations, the thick line to Eq. (117). $\hat{r}_0^{IF}$ [Eq. (99)] is also plotted (dashed line) and in this low noise regime almost coincides with Eq. (117) except in a very small region at low frequency (see insets).

Using $Y(\omega)$ defined in Eq. (100), one obtains

$$g_1\hat{w}_1=\frac{\gamma Y(0)}{1+i\omega\tau_1+\gamma Y(0)}, \tag{113}$$

where

$$Y(0)=1-(y_\theta-y_r)\,\tau\hat{r}_0^{IF}(\omega=0) \tag{114}$$

and $\hat{r}_0^{IF}(\omega=0)$ is given explicitly in Eq. (101). The firing-rate modulation in the low frequency regime is given by Eqs. (107) and (113)

$$\hat{r}_0(\omega)=\frac{1+i\omega\tau_1}{1+i\omega\tau_1+\gamma Y(0)}\hat{r}_0^{IF}(\omega=0). \tag{115}$$

An expression that interpolates between the low and high frequency regimes is simply

$$\hat{r}_0(\omega)=\frac{1+i\omega\tau_1}{1+i\omega\tau_1+\gamma Y(0)}\hat{r}_0^{IF}(\omega). \tag{116}$$

A slightly different interpolating expression was proposed in Sec. IV A 2. It is obtained by keeping the $-i\omega\hat{P}_0\tau$ term in Eq. (105). This simply replaces $\hat{Q}_0^{IF}(y;\omega=0)$ by $\hat{Q}_0^{IF}(y;\omega)$ in each step from Eq. (105) to Eq. (116) and it leads to the alternative formula

$$\hat{r}_0^{sc}(\omega)=\frac{1+i\omega\tau_1}{1+i\omega\tau_1+\gamma Y(\omega)}\hat{r}_0^{IF}(\omega), \tag{117}$$

with $Y(\omega)$ defined by Eq. (100) and $\hat{r}_0^{IF}(w)$ given by Eq. (99).

The analytical formulas are compared to results of direct numerical simulations in Figs. 9 and 10. For these parameter values, the two formulas of Eq. (116) and (117) are numerically very close and describe quite well the numerical results.

C. Unmasking of the subthreshold resonance by noise

In high noise conditions, the firing-rate resonance curve is peaked around the subthreshold frequency as seen in Figs. 7(C) and 9. The corresponding resonance curves in low noise conditions with the same average firing-rate (obtained by increasing the injected current I_0) are shown in Figs. 7(A) and 10. They display a strong resonance peak at the firing-rate frequency and peaks of lower amplitude at its harmonics, attenuated but recognizable features of the firing-rate resonance curves in the deterministic limit (compare with Fig. 5). Figures 9 and 10 also show that the GIF response $\hat{r}_0(\omega)$ at low frequencies can be either smaller than the leaky IF response $\hat{r}_0^{IF}$ (hence creation of a peak around subthreshold frequency, see Fig. 9) or higher than the leaky IF response (hence a trough around subthreshold frequency, see inset in Fig. 10). The condition that determines whether a peak or a trough is present can be obtained from Eq. (117). A peak is found for $Y(0)>0$, while a trough is found for $Y(0)<0$. Alternatively, this condition can be obtained from the slope of the *f-I* curve, since $Y(0)$ is linearly related to $\hat{r}_0^{IF}(\omega=0)$. For a slope larger than $1/[C(\theta-V_r)]$, a peak is obtained in the firing-rate response, and a trough otherwise. Note that $1/[C(\theta-V_r)]$ is the slope that is obtained in the high firing-rate limit in the absence of a refractory period. Thus, the qualitative behavior of the firing-rate response at low frequency can be obtained by an inspection of the *f-I* curves shown in Fig. 8. For low noise levels, the slope is small at low firing-rates (hence a peak at subthreshold frequency), then increases above its asymptotic value (hence a trough at subthreshold frequency), and then decreases towards its asymptotic value (the trough becomes less and less pronounced as firing-rates increase). For high noise levels, the slope is always smaller than its asymptotic value, which means that a peak at subthreshold frequency is always present, but the peak should vanish at very large rates.

For the parameter values of Figs. 9 and 10, the peak of the firing-rate resonance curve is plotted in Fig. 11 as a function of the noise intensity. This clearly illustrates the peak shift from the firing-rate frequency to the subthreshold preferred frequency with increasing noise. Thus, noise helps to uncover a resonant peak at the subthreshold preferred frequency in the firing-rate response. In some sense, this might be considered as a form of stochastic resonance [19]. However, this phenomenon is very different from previously discussed stochastic resonance phenomena in neurons (see, e.g., Ref. [27]). These studies considered the spectrum of the interspike interval distribution (ISI) of a neuron subjected to a noisy sinusoidal current as the quantity of interest. What was shown in a variety of models, including the leaky integrate-and-fire neuron, is that the signal-to-noise ratio (SNR) of the transmitted frequency exhibits a peak at some positive noise level. Here, we have considered a very different quantity, the linear response of the instantaneous firing-rate. This measure is more appropriate in the context of the transmission of an oscillatory signal at the network level. It is also one of the main quantities that determines whether a network is asynchronous or not (see, e.g., Ref. [17]). The behavior of this measure is quite different from the SNR of the ISI distribu-

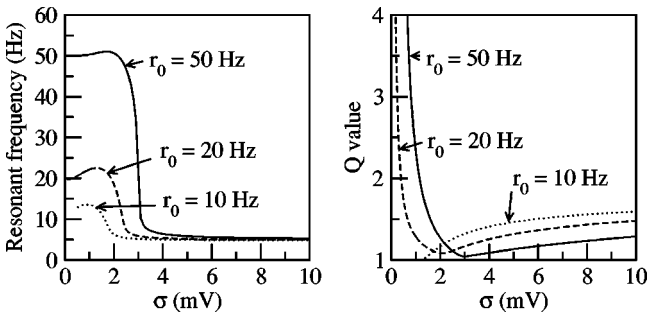

FIG. 11. Dependence on noise of location ω_{pfr} of the peak of firing-rate response, for three values of the background rate, 10, 20, and 50 Hz. At each noise level σ, current I_0 is adjusted to leave the firing rate constant at the desired value, using Eq. (92) (other parameters as in Fig. 9). The left panel shows the rather abrupt transition of the peak from the firing-rate frequency to the subthreshold resonance frequency (about 5 Hz here) as noise is increased and current I_0 is decreased. The right panel shows the Q value of the resonance defined as the ratio of the modulation at the peak frequency ω_{pfr} over the modulation at zero frequency. $|\hat{r}(\omega_{pfr})/\hat{r}(0)|$. For $r_0=10$ Hz, Q is less than 1 when curve $|\hat{r}(\omega)|$ has a large negative slope at the origin [due to the high slope of the $r_s(I_0)$ curve].

tion. In the suprathreshold firing regime, noise decreases the relative size of the resonant peak at the firing frequency, in both IF and GIF neurons, in a monotonic way. In the subthreshold firing regime, noise enhances in a monotonic way the relative size of the resonant peak at the subthreshold preferred frequency, if the firing rate is kept constant as noise is varied. This behavior occurs in GIF neurons with subthreshold resonance, but not in IF neurons that have no subthreshold preferred frequency.

V. CONCLUSIONS AND PERSPECTIVES

In this paper, a generalized integrate-and-fire model has been studied in order to shed light on the relation between subthreshold resonance and firing-rate modulation.

It had been shown in a previous study [12] using both the GIF model and conductance-based modeling that a sufficiently large amount of noise was necessary for the subthreshold resonance to be able to create a firing-rate resonance. The present study provides a detailed analysis of this phenomenon for the two-variable GIF model. For noiseless and weak noise inputs, the results of Secs. II and IV show that the firing-rate modulation is strongest at the firing-rate frequency (and its harmonics) and that there is a *trough* in the response at frequencies around the subthreshold frequency. Contrary to this, for sufficiently noisy inputs, the results of Sec. IV show that the resonance of the firing-rate stands around the subthreshold frequency and the perturbative results describe well the numerical data. In the present paper, we have illustrated in Figs. 5, 7, 9, and 10 the situation in which the background firing rate is larger than the subthreshold preferred frequency. The two variable resonant GIF neurons are type II and their minimal firing rate in the absence of noise cannot be much smaller than the subthreshold resonant frequency. Hence, the situation in which the firing rate is smaller than the subthreshold frequency can be achieved, in practice, only with noise and, in this regime, the firing-rate amplifies preferentially inputs at the subthreshold resonant frequency [12].

As regards the mathematical treatment of the two-variable GIF model, the main results have been obtained perturbatively in the limit where the supplementary variable is slow as compared to the membrane potential dynamics. It is worth emphasizing that this is relevant for the description of many real cells. From the multiple cell types that exhibit resonance in the nervous system, most show resonance at frequencies of a few Hertz. Neurons in the inferior olive [28,29] and in the thalamus [30,31] show resonance at about 4 Hz. Pyramidal cells in the neocortex can show resonance at 1–2 Hz at hyperpolarized levels [5] or 5–20 Hz at more depolarized levels [6]. Finally, pyramidal cells in the hippocampus also show resonance at low frequencies in the θ band (2–7 Hz, [7,8]). Such frequencies can be obtained with a time constant of the ''activation variable'' w around $\tau_1 \sim 100$ ms. It is interesting to note that for such values of τ_1, the small τ/τ_1 expansion gives a very good approximation of the reduced model behavior (see Figs. 9 and 10). The reduced model itself often gives a very good approximation of the behavior of more realistic conductance-based cells [12].

Other approximate treatments can probably be developed to describe different parameter regimes. Several cells show resonance at higher frequencies. For instance, interneurons of the hippocampus show resonance in the γ band (30–50 Hz, [8]). Such frequencies are obtained with smaller time constants τ_1 and hence the small τ/τ_1 expansion gives less accurate results. However, the difference between simulations and analytical data seem to be accounted well by a frequency-independent multiplicative factor. It thus seems that no qualitatively new phenomenon arises from the higher-order terms, at least in the range of the values of τ_1 investigated here (10–200 ms). Obtaining the exact solution of the problem would nevertheless be interesting but appears rather difficult.

The main features observed in simulations of more realistic models [12] are similar to those obtained with the GIF model and can thus be described by the present analysis. Several simplifying assumptions made in the formulation of the GIF model should, however, be noted. The most obvious ones are that the GIF model subthreshold properties are independent of the membrane potential and that spike-generating dynamics is absent. Numerical results using conductance-based models [12] show that the basic phenomenon is independent of these simplifications. It could nonetheless be worthwhile to try and develop a direct analysis of these more realistic models.

A second set of simplifications pertains not to the neuron dynamics itself but to the modeling of its inputs. It has been chosen here for simplicity to consider a white noise current source. While this could be studied in an experiment in isolated cells or in a slice, this certainly greatly simplifies synaptic inputs in at least two important respects. They are better modeled as conductance modifications and, furthermore, noise is colored on the time scale of the synaptic dynamics [33]. It is known that the replacement of white noise by

colored noise can modify the response of neurons at high frequency [25]. Again, the numerical results of Ref. [12] indicate that the qualitative phenomenon is preserved in this more complicated case, but a more quantitative analysis might be worth pursuing.

It is certainly of great interest to understand how the properties of individual cells affect the collective properties of networks of cells. The present study may help in two ways to make progress in this direction. First, at a purely numerical level, the IF neuron has proven very useful as the simplest spiking neuron model and it has been widely used as the elementary component of large network simulations. The GIF neuron should provide the appropriate substitute and permit the incorporation of key features of the subthreshold response. In networks of inhibitory leaky integrate-and-fire neurons, noise has previously been shown to give rise to oscillatory modes in which neurons fire irregularly at low rates, while the population activity oscillates at a frequency determined by the synaptic time constants [17,34,35]. It will be interesting to investigate whether networks of cells with more realistic subthreshold dynamics, such as the GIF model studied here, can give rise to new oscillatory modes. At a more theoretical level, the linear firing-rate response of the neuron that was determined here is a key quantity in the analysis of this question and the determination of the conditions of network oscillations, as was shown for networks of leaky integrate-and-fire neurons [17,35] and for networks of excitatory neurons with adaptation currents [36]. The results of the present paper show that noise will potentially play a strong role in shaping the synchronization properties of networks of neurons with subthreshold resonance. This should allow for an analysis of the respective roles of intrinsic and synaptic dynamics in the collective behavior of large networks and allow for an assessment of the functional role of subthreshold resonance in neural systems.

ACKNOWLEDGMENTS

We would like to thank O. Paulsen for useful discussions. M.J.E.R. acknowledges support from the European Union.

APPENDIX: FIRST CORRECTION TO THE FIRING RATE IN THE LARGE τ_1 EXPANSION

The formalism of Sec. IV B can be used to obtain higher-order corrections to the lowest-order results given in the main text in a systematic way. This is illustrated here by deriving the first correction to the steady firing-rate both for the zero-leak case and for the general $g \neq 0$ case. The zero-leak case is treated separately because much more explicit expressions can be obtained. This also serves to illustrate a method of calculation that avoids the explicit computation of the probability distribution by focusing on its moments.

1. The zero-leak case and the moment method

The aim is to calculate the first higher-order correction to the firing-rate for the simple case of $g=0$. The regime of interest is that for which β is large and, therefore, the corrections will be sought in the form of a series of inverse powers of $\sqrt{\beta}$. The time-independent Fokker-Planck equation (44) for this case is

$$0=\frac{\Delta}{2C^2}\frac{\partial^2 P}{\partial v^2}+\frac{1}{C}\frac{\partial}{\partial v}[(g_1 w-I_0)P]+\frac{1}{\tau_1}\frac{\partial}{\partial w}[(w-v)P].$$

The substitutions $v=\overline{w}+x\sqrt{\Delta/Cg_1}$ and $w=\overline{w}+z\beta^{-1/2}\sqrt{\Delta/Cg_1}$ are made, yielding the reduced-variable Fokker-Planck equation:

$$0=\frac{1}{2}\frac{\partial^2 P}{\partial x^2}+\frac{\zeta}{2}\frac{\partial P}{\partial x}+\frac{1}{\sqrt{\beta}}\left(z\frac{\partial P}{\partial x}-x\frac{\partial P}{\partial z}\right)+\frac{1}{\beta}\frac{\partial}{\partial z}(zP), \tag{A1}$$

with ζ defined by

$$\zeta=2\sqrt{\frac{C}{\Delta g_1}}(g_1\overline{w}-I_0).$$

Note that in this section, the normalization of z is different by a factor of $\sqrt{g/g_1}$ from that chosen in the rest of this paper (which is not compatible with $g=0$).

The first correction to the firing-rate can be conveniently obtained by taking various moments of Eq. (A1). To this end, multiplying by a factor $x^m z^n$ and integrating over the space of the x and z variables gives

$$\rho(z^n)(x_0^m-x_r^m)+m(m-1)\langle x^{m-2}z^n\rangle=m\zeta\langle x^{m-1}z^n\rangle + \frac{2m}{\sqrt{\beta}}\langle x^{m-1}z^{n+1}\rangle-\frac{2n}{\sqrt{\beta}}\langle x^{m+1}z^{n-1}\rangle+\frac{2n}{\beta}\langle x^m z^n\rangle, \tag{A2}$$

where the following definitions have been used:

$$\langle A\rangle=\int_{-\infty}^{\infty}dz\int_{-\infty}^{x_0}dxAP,$$

$$\rho(z^n)=\int_{-\infty}^{\infty}dz z^n\left.\frac{\partial P}{\partial x}\right|_{x_0}\quad\text{with}\quad\rho=\rho(1),$$

$$x_0=\sqrt{\frac{Cg_1}{\Delta}}(\theta-\overline{w})\quad\text{and}\quad x_r=\sqrt{\frac{Cg_1}{\Delta}}(V_r-\overline{w}). \tag{A3}$$

Putting $m=0$ in Eq. (A2) gives

$$\langle xz^{n-1}\rangle=\frac{1}{\sqrt{\beta}}\langle z^n\rangle\quad\text{for}\quad n\geq 1. \tag{A4}$$

This equation (with $n=1$) states that, to leading order, $\langle x\rangle \sim 1/\sqrt{\beta}$. For $n=0$, with $m=1$ and $m=2$, Eq. (A2) becomes

$$(x_0-x_r)\rho=\zeta+\frac{2}{\sqrt{\beta}}\langle z\rangle, \tag{A5}$$

$$(x_0^2-x_r^2)\rho+2=2\zeta\langle x\rangle+\frac{4}{\sqrt{\beta}}\langle xz\rangle, \tag{A6}$$

respectively. On substituting for ρ, these two equations give to zero order

$$\zeta=-\frac{2}{(x_0+x_r)}. \tag{A7}$$

Using the definitions of ζ, x_0, and x_r, Eq. (A7) gives a quadratic equation for $\overline{w}$. The root that is consistent with the normalization condition on the probability density can be shown to be $\overline{w}=\langle v\rangle$ [Eq. (52)]. As expected, this zero-order result is equivalent to the self-consistent replacement: $w\rightarrow\langle v\rangle$. The choice is made to enforce relation (A7) to all orders (this can be taken as a definition of shift $\overline{w}$).

From the moment equation with $m=1$ and $n=0$, constant ρ (which is related to the firing-rate) is given by

$$\rho=\frac{\zeta}{x_0-x_r}\left(1+\frac{2}{\sqrt{\beta}}\frac{\langle z\rangle}{\zeta}\right).$$

It remains only to obtain $\langle z\rangle$ to leading order. This can be achieved by using the moment equation (A2) with $m=1$ and $m=2$:

$$\rho\langle z^n\rangle(x_0-x_r)=\zeta\langle z^n\rangle+\frac{2}{\sqrt{\beta}}\langle z^{n+1}\rangle-\frac{2n}{\sqrt{\beta}}\langle x^2z^{n-1}\rangle+\frac{2n}{\beta}\langle xz^n\rangle, \tag{A8}$$

$$\rho\langle z^n\rangle(x_0^2-x_r^2)+2\langle z^n\rangle=2\zeta\langle xz^n\rangle+\frac{4}{\sqrt{\beta}}\langle xz^{n+1}\rangle-\frac{2n}{\sqrt{\beta}}\langle x^3z^{n-1}\rangle+\frac{2n}{\beta}\langle x^2z^n\rangle. \tag{A9}$$

On multiplying Eq. (A8) by 2 and Eq. (A9) by ζ and adding them to eliminate $\rho\langle z^n\rangle$ using Eq. (A7), the following is obtained:

$$n\zeta\langle x^3z^{n-1}\rangle+2n\langle x^2z^{n-1}\rangle=\left(2+\zeta^2+\frac{2n}{\beta}\right)\langle z^{n+1}\rangle+\frac{2\zeta}{\sqrt{\beta}}\langle z^{n+2}\rangle+\frac{n\zeta}{\sqrt{\beta}}\langle x^2z^n\rangle, \tag{A10}$$

where relation (A4) has also been used. With $n=0$, this equation yields

$$\langle z\rangle=-\frac{1}{\sqrt{\beta}}\frac{2\zeta\langle z^2\rangle}{(2+\zeta^2)} \tag{A11}$$

and with $n=1$,

$$\left(2+\zeta^2+\frac{2}{\beta}\right)\langle z^2\rangle=\zeta\langle x^3\rangle+2\langle x^2\rangle-\frac{2\zeta}{\sqrt{\beta}}\langle z^3\rangle-\frac{\zeta}{\sqrt{\beta}}\langle x^2z\rangle. \tag{A12}$$

The last result implies that, to zero order,

$$\langle z^2\rangle_0=\frac{(\zeta\langle x^3\rangle_0+2\langle x^2\rangle_0)}{(2+\zeta^2)}. \tag{A13}$$

The zero-order forms of Eq. (A2) with $m=1,2,3,4$ and $n=0$ can be used to obtain $\langle x^2\rangle_0$ and $\langle x^3\rangle_0$:

$$\langle x^2\rangle_0=\frac{1}{3}\left(\frac{x_0^3-x_r^3}{x_0-x_r}\right)=\frac{1}{3}(x_0^2+x_0x_r+x_r^2)$$

$$\langle x^3\rangle_0=\frac{1}{4}\left(\frac{x_0^4-x_r^4}{x_0-x_r}\right)+\frac{1}{\zeta}\left(\frac{x_0^3-x_r^3}{x_0-x_r}\right)=-\frac{1}{4}(x_0+x_r)^3.$$

Combining these results and noting the relation between ρ and the firing-rate $r=-g_1\rho/2C$ gives

$$r=r_0\left(1-\frac{1}{\beta}\frac{4\langle z^2\rangle_0}{(2+\zeta^2)}\right)=r_0\left(1-\frac{4}{\beta}\frac{(\zeta\langle x^3\rangle_0+2\langle x^2\rangle_0)}{(2+\zeta^2)^2}\right) \tag{A14}$$

as the order $1/\beta$ correction to the firing-rate. The zero-order firing-rate $r_0=g_1/[C(x_0^2-x_r^2)]$ is equivalent to the result given in Eq. (53).

2. The first-order correction in the general case

The starting point is the Fokker-Planck equation (83). Inserting the series expansion, Eq. (92), in Eq. (83), gives the successive orders in P,

$$LP_0=0, \tag{A15}$$

$$LP_1=-\gamma\left(z\frac{\partial P_0}{\partial y}+(\overline{y}-y)\frac{\partial P_0}{\partial z}\right), \tag{A16}$$

$$LP_2=-\gamma\left(z\frac{\partial P_1}{\partial y}+(\overline{y}-y)\frac{\partial P_1}{\partial z}+\frac{\partial}{\partial z}(zP_0)\right), \tag{A17}$$

$$LP_3=-\gamma\left(z\frac{\partial P_2}{\partial y}+(\overline{y}-y)\frac{\partial P_2}{\partial z}+\frac{\partial}{\partial z}(zP_1)\right), \tag{A18}$$

where the linear operator L is defined by

$$LP=\frac{1}{2}\frac{\partial^2P}{\partial y^2}+\frac{\partial}{\partial y}(yP). \tag{A19}$$

We note that functions P_i must be even (odd) in z for even (odd) orders i. This implies that the corrections to the firing rate at odd orders are zero, since the firing rate is obtained by integrating P over z at $y=y_\theta$ [Eq. (46)].

The solution to equation (A15) that satisfies the boundary conditions is given by Eq. (89),

$$P_0(y,z)=2r_0(z)Q_0(y), \tag{A20}$$

$$Q_0(y)=e^{-y^2}\int_y^{y_\theta} e^{u^2}\Theta(u-y_r)du, \tag{A21}$$

$$r_0\tau=\int_{-\infty}^{+\infty} r_0(z)dz=\left(2\int_{-\infty}^{y_\theta} Q_0(y)dy\right)^{-1}, \tag{A22}$$

where $r_0(z)$ is determined by a solvability condition [see Eq. (A28) below] for the second-order Eq. (A17).

The solution to Eq. (A16) that satisfies the boundary conditions is

$$P_1(y,z)=2r_1(z)Q_0(y)+4\gamma[zr_0(z)JQ_0(y) - r_0'(z)JKQ_0(y)], \tag{A23}$$

where J and K are operators defined by

$$Jf(x)=\exp(-x^2)\int_x^{y_\theta}\exp(u^2)f(u)du, \tag{A24}$$

$$Kf(x)=\int_{-\infty}^{x}(u-\overline{y})f(u)du, \tag{A25}$$

and $r_1(z)$ is defined by Eq. (87) and is determined by a solvability condition on the third-order Eq. (A18) [Eq. (A33) below].

The solution to Eq. (A16) that satisfies the boundary conditions is

$$\begin{aligned}P_2(y,z)=&2r_2(z)Q_0(y)+4\gamma\{zr_1(z)JQ_0(y)\\ &-r_1'(z)JKQ_0(y)+[zr_0(z)]'JIQ_0(y)\}\\ &+8\gamma^2\{z^2r_0(z)J^2Q_0(y)-zr_0'(z)J^2KQ_0(y)\\ &-[zr_0(z)]'JKJQ_0(y)\}+8\gamma^2r_0''JKJKQ_0(y),\end{aligned} \tag{A26}$$

where

$$If(x)=\int_{-\infty}^{x} f(u)du \tag{A27}$$

and an additional condition must be imposed on $r_0(z)$ to satisfy the boundary conditions:

$$4\gamma KJKQ_0(y_\theta)\frac{\partial^2 r_0}{\partial z^2}+\left(\frac{1}{r_0\tau}-4\gamma KJQ_0(y_\theta)\right)\frac{\partial}{\partial z}(zr_0)=0. \tag{A28}$$

This condition gives $r_0(z)$:

$$r_0(z)=\frac{r_0\tau}{\sqrt{2\pi\langle z^2\rangle_0}}\exp\left(-\frac{z^2}{2\langle z^2\rangle_0}\right), \tag{A29}$$

$$\langle z^2\rangle_0=\frac{4\gamma KJKQ_0(y_\theta)}{\dfrac{1}{r_0\tau}-4\gamma KJQ_0(y_\theta)}. \tag{A30}$$

Condition $\int_{-\infty}^{y_\theta}dy\int_{-\infty}^{+\infty}dz\,P_2(y,z)=0$ gives r_2,

$$\begin{aligned}r_2=-4\gamma r_0\Bigg(&IJQ_0(y_\theta)\int_{-\infty}^{+\infty}dzzr_1(z)+2\gamma r_0\tau IJ^2KQ_0(y_\theta)\\ &+2\gamma r_0\tau\langle z^2\rangle_0 IJ^2Q_0(y_\theta)\Bigg).\end{aligned} \tag{A31}$$

Thus, we still need to determine $\int_{-\infty}^{+\infty}dzzr_1(z)$ to obtain the first nonzero correction to the firing-rate r_2. Integrating both sides of Eq. (A18) provides the solvability condition at third order,

$$\int_{-\infty}^{y_\theta}dy\left((\overline{y}-y)\frac{\partial P_2}{\partial z}+\frac{\partial}{\partial z}(zP_1)\right)=0. \tag{A32}$$

With the previous expressions (A23) and (A26) for P_1 and P_2, this gives an inhomogeneous second-order ordinary differential equation, which determines $r_1(z)$,

$$\begin{aligned}&4\gamma KJKQ_0(y_\theta)\frac{\partial^2 r_1}{\partial z^2}+\left(\frac{1}{r_0\tau}-4\gamma KJQ_0(y_\theta)\right)\frac{\partial}{\partial z}(zr_1)\\ &=r_0'''\{8\gamma^2KJKJKQ_0(y_\theta)+4\gamma\langle z^2\rangle_0[2\gamma KJKJQ_0(y_\theta)\\ &\quad-KJIQ_0(y_\theta)]\}+(z^2r_0)'\Bigg[2\gamma(4\gamma KJ^2Q_0(y_\theta)\\ &\quad-2IJQ_0(y_\theta))+4\gamma\frac{2\gamma KJ^2KQ_0(y_\theta)-IJKQ_0(y_\theta)}{\langle z^2\rangle_0}\Bigg].\end{aligned} \tag{A33}$$

Solution $r_1(z)$ is equal to $r_0(z)$ times a polynomial in z containing only terms in z^3 and z. The first moment is directly obtained by integrating Eq. (A33) twice over z,

$$\begin{aligned}\int_{-\infty}^{+\infty}dzzr_1(z)=\langle z^2\rangle_0\Bigg[&2\gamma\left(\frac{4\gamma KJ^2Q_0-2IJQ_0}{\dfrac{1}{r_0\tau}-4\gamma KJQ_0}\right)\\ &+\left(\frac{2\gamma KJ^2KQ_0-IJKQ_0}{KJKQ_0}\right)\Bigg]_{y=y_\theta}.\end{aligned} \tag{A34}$$

[1] C. Koch and I. Segev, *Methods in Neuronal Modeling: From Ions to Networks*, 2nd ed. (MIT Press, Cambridge, MA, 1998).
[2] P. Dayan and L.F. Abbott, *Theoretical Neuroscience* (MIT Press, Cambridge, MA, 2001).
[3] E. Salinas and T.J. Sejnowski, Nat. Rev. Neurosci. **2**, 539 (2001); X.-J. Wang, *Encyclopedia of Cognitive Science* (Macmillan, London, 2002), and references therein.
[4] E. Puil, B. Gimbarzevsky, and R.M. Miura, J. Neurophysiol. **55**, 995 (1986).
[5] B. Hutcheon, R.M. Miura, and E. Puil, J. Neurophysiol. **76**, 683 (1996); **76**, 698 (1996).
[6] Y. Gutfreund, Y. Yarom, and I. Segev, J. Physiol. **483**, 621 (1995).
[7] L.S. Leung and H.W. Yu, J. Neurophysiol. **79**, 1592 (1998).
[8] F.G. Pike *et al.*, J. Physiol. **529**, 205 (2000).
[9] See B. Hutcheon and Y. Yarom, Trends Neurosci. **23**, 216 (2000), and references therein.
[10] A.L. Hodgkin and A.F. Huxley, J. Physiol. **117**, 500 (1952).
[11] C. Koch, *Biophysics of Computation* (Oxford University Press, Oxford, 1999).
[12] M.J.E. Richardson, N. Brunel, and V. Hakim, J. Neurophysiol. **89**, 2538 (2003).
[13] L. Lapicque, J. Physiol. Pathol. Gen. **9**, 620 (1907).
[14] H. Tuckwell, *Introduction to Theoretical Neurobiology* (Cambridge University Press, Cambridge, 1988).
[15] A. Treves, Network **4**, 259 (1993).
[16] L.F. Abbott and C. van Vreeswijk, Phys. Rev. E **48**, 1483 (1993).
[17] N. Brunel and V. Hakim, Neural Comput. **11**, 1621 (1999).
[18] A related model has been proposed in E.M. Izhikevich, Neural Networks **14**, 883 (2001).
[19] R. Benzi, A. Sutera, and A. Vulpiani, J. Phys. A **14**, L453 (1981); see K. Wiesenfeld and F. Moss, Nature (London) **373**, 33 (1995), and references therein for a short overview of applications in life sciences.
[20] A.R. Bulsara, S.B. Lowen, and C.D. Rees, Phys. Rev. E **49**, 4989 (1994).
[21] W. Gerstner, Neural Comput. **12**, 43 (2000).
[22] B.W. Knight, J. Gen. Physiol. **59**, 734 (1972).
[23] B.W. Knight, A. Omurtag, and L. Sirovich, Neural Comput. **12**, 1045 (2000).
[24] D.Q. Nykamp and D. Tranchina, J. Comput. Neurosci. **8**, 19 (2000).
[25] N. Brunel, F.S. Chance, N. Fourcaud, and L.F. Abbott, Phys. Rev. Lett. **86**, 2186 (2001).
[26] S. Chandrasekhar, Rev. Mod. Phys. **15**, 1 (1943).
[27] H.E. Plesser and T. Geisel, Phys. Rev. E **59**, 7008 (1999).
[28] I. Lampl and Y. Yarom, Neuroscience **78**, 325 (1997).
[29] C.I. De Zeeuw *et al.*, Trends Neurosci. **21**, 391 (1998).
[30] H. Jahnsen and S. Karnup, Brain Res. **666**, 9 (1994).
[31] E. Puil, H. Meiri, and Y. Yarom, J. Neurophysiol. **71**, 575 (1994).
[32] *Tables of Mathematical Functions*, edited by M. Abramovitz and I.A. Stegun (Dover, New York, 1972); Kummer's function can be defined as a power series, $M(a,b,x)=1+ax/b+a(a+1)/b(b+1)x^2/2!+\cdots$.
[33] See, e.g., A. Destexhe, M. Rudolph, J.-M. Fellous, and T.J. Sejnowski, Neuroscience **107**, 13 (2001), for a discussion and a simple modeling.
[34] P.H.E. Tiesinga and J.V. Jose, Network **11**, 1 (2000).
[35] N. Brunel and X.-J. Wang, J. Neurophysiol. (to be published).
[36] G. Fuhrmann, H. Markram, and M. Tsodyks, J. Neurophysiol. **88**, 761 (2002).
[37] See, e.g., M.I. Freidlin and A.D. Wentzell, *Random Perturbations of Dynamical Systems* (Springer, New York, 1984), for the general formalism; M.-L. Chabanol, V. Hakim, and W.-J. Rappel, Physica D **103**, 273 (1997), for an explicit computation in a similar case.